Three-dimensional structures and elemental distributions of Stardust impact tracks using synchrotron microtomography and X-ray fluorescence analysis

A. TSUCHIYAMA[1]*, T. NAKAMURA[2], T. OKAZAKI[1], K. UESUGI[3], T. NAKANO[4], K. SAKAMOTO[2], T. AKAKI[2], Y. IIDA[1], T. KADONO[5], K. JOGO[2], and Y. SUZUKI[3]

[1]Department of Earth and Space Science, Graduate School of Science, Osaka University, Toyonaka 560-0043, Japan
[2]Department of Earth and Planetary Science, Faculty of Sciences, Kyushu University, Hakozaki, Fukuoka 812-8581, Japan
[3]Synchrotron Radiation Research Institute, Spring-8, Sayo, Hyogo 679-5198, Japan
[4]Geological Survey of Japan, Advanced Industrial Science and Technology, Tsukuba 305-8567, Japan
[5]Institute of Laser Engineering, Osaka University, Suita 565-0871, Japan
*Corresponding author. E-mail: akira@ess.sci.osaka-u.ac.jp

Abstract–Three-dimensional structures and elemental abundances of four impact tracks in silica aerogel keystones of Stardust samples from comet 81P/Wild 2 (bulbous track 67 and carrot-type tracks 46, 47, and 68) were examined non-destructively by synchrotron radiation-based microtomography and X-ray fluorescence analysis. Track features, such as lengths, volumes and width as a function of track depth, were obtained quantitatively by tomography. A bulbous portion was present near the track entrance even in carrot-type tracks. Each impact of a cometary dust particle results in the particle disaggregated into small pieces that were widely distributed on the track walls as well as at its terminal. Fe, S, Ca, Ni, and eight minor elements are concentrated in the bulbous portion of track 68 as well as in terminal grains. It was confirmed that bulbous portions and thin tracks were formed by disaggregation of very fine fragile materials and relatively coarse crystalline particles, respectively. The almost constant ratio of whole Fe mass to track volume indicates that the track volume is almost proportional to the impact kinetic energy. The size of the original impactor was estimated from the absolute Fe mass by assuming its Fe content (CI) and bulk density. Relations between the track sizes normalized by the impactor size and impact conditions are roughly consistent with those of previous hypervelocity impact experiments.

INTRODUCTION

Samples directly derived from a comet have fundamental importance to our understanding of the early solar nebula and protoplanetary history, particularly in combination with the study of interplanetary dust particles (IDPs). Particles from comet 81P/Wild 2 have been successfully recovered by using silica aerogel collectors in the Stardust mission (Brownlee et al. 2006). Preliminary examination of impact tracks in the aerogels formed during cosmic dust capture showed that they have a variety of morphologies, from carrot-shaped to bulbous, and sizes, suggesting a diversity of cometary dust impactors (Brownlee et al. 2006; Hörz et al. 2006). Diversity is also suggested by the morphology of craters on aluminum foils on the dust collector (Hörz et al. 2006; Kearsley et al. 2008). The impacting particles were disaggregated into grains (<a few tens of μm) distributed along the tracks (Brownlee et al. 2006). It has been proposed that the particles were

originally mixtures of very fine fragile material and relatively coarse crystalline particles (Nakamura et al. 2008a), and these loose aggregates were disaggregated into individual components with the larger, denser components penetrating more deeply into the aerogel, making thin tracks with terminal grains (Zolensky et al. 2006). The elemental abundances of the whole original dust particles, integrated along entire tracks, are almost chondritic, but the elements are distributed heterogeneously along the tracks (Flynn et al. 2006). The isotopic compositions are consistent with most of the materials having a solar system origin (McKeegan et al. 2006). Organic materials of heterogeneous and unequilibrated distribution in abundance and composition were also found (Sandford et al. 2006; Keller et al. 2006).

Discovery of crystalline particles formed at high temperatures, such as CAI (Zolensky et al. 2006) and chondrule-like materials (Nakamura et al. 2008b), provide new scope for solar system formation (Ciesla et al. 2007). In

Table 1. Summary of impact tracks by microtomography.

Track #	Allocation	Type[*]	Track length, L_t (μm)	Track volume, V_t (μm^3)	Track entrance (mm)[$]	Max. track diameter, D_m (μm)	Compacted aerogel volume, V_{ca} (μm^3)	Sum of large grain volumes, ΣV_g (μm^3)	Track length, $L_{t,calc}$ (μm)[#]	Remarks
Track 67	C2126,1,67,0 (Namekuji)	C	114	4.55E + 04	7.6 × 4.1	31.9	1.43E + 04	n.d.	6150	
Track 68	C2126,2,68,0 (Skyrocket)	A	2656	9.17E + 06	85.0 × 64.4	148	2.49E + 06	3.80E + 04	40800	Bifurcated[†]
Track 46	C2126,4,46,0 (Gobou)	A	⩾953	⩾1.96E + 05	46.0 × 31.9	32.6	8.68E + 04	n.d.	8630	Terminal particle lost
Track 47	FC13,2,47,0	A	n.d.	n.d.	n.d.	n.d.	n.d.	n.d.	n.d.	Partly destroyed

[*]Type A: carrot-like, Type C: bulbous and stubby cavity (Hörz et al. 2006).

[$]Track entrance hole size measured roughly at the aerogel surface.

[#]Calculation based on Dominguez et al. (2004).

[†]Lengths of subtracks from the entrance: 1788, 1446, 1184, 1098, 809 μm.

n.d.: not determined.

contrast, very fine fragile materials, which are considered to be pristine cometary materials, were mixed with large amounts of melted aerogel (Nakamura et al. 2008a; Rietmeijer et al. 2008), and their original information was obtained with great difficulty. Ishii et al. (2008) proposed that the fine-grained materials are different from anhydrous IDPs, which are considered to have cometary origins.

Hörz et al. (2006) discussed impact features of the tracks from their morphologies using optical microscopy. The size distribution of Wild 2 dust (from tens of nm to hundreds of μm in size) was estimated from the track widths based on hypervelocity impact experiments into low density materials (Hörz et al. 2006; Burchell et al. 2008). Track size parameters, such as length, width and volume, have been measured under an optical microscope. Although this conventional method gives statistical data, the measured values are rough, and details of track shapes cannot be obtained.

We have investigated three-dimensional structures and elemental distributions of impact tracks by non-destructive X-ray analyses (microradiography, microtomography, and X-ray fluorescence (XRF) analysis) using synchrotron radiation (SR) as members of the preliminary examination team (PET) of the Stardust samples. SR-tomography (e.g., Uesugi et al. 2001, 2003; Tsuchiyama et al. 2005) can give three-dimensional (3-D) structures of tracks in aerogels in detail and quantitatively. If the technique is combined with SR-based XRF for the same samples in the same sample stage setting, we can obtain quantitative relationships between track morphologies and chemical compositions. This study gives useful information on the physical and chemical conditions of the dust capture process and clues to understanding the nature of the original cometary material, especially for fine-grained materials and relatively coarse particles. In this study, the original dust sizes were also estimated from the iron contents of the tracks independent of

the track morphology. This makes possible comparison of Stardust track formation with experimental and theoretical studies on track formation (e.g., Kadono 1999; Dominguez et al. 2004; Burchell et al. 2008; Trigo-Rodriguez et al. 2008).

EXPERIMENTS

Four keystones having impact tracks of Stardust samples were examined in this study: track 67: C2126,1,67,0 (bulbous and stubby cavity, ~0.1 mm long), track 68: C2126,2,68,0 (carrot-shaped with bifurcated thin tracks, ~2.7 mm long), track 46: C2126,4,46,0 (carrot-shaped, ~1.0 mm long), and track 47: FC13,2,47,0 (carrot-shaped, ~0.3 mm long) (Table 1; Fig. 1). On the basis of track morphologies, the former three tracks were named Namekuji (slug), Skyrocket, and Gobou (burdock), respectively.

The samples were analyzed at beamline BL47XU of SPring-8, Japan. Figure 2 shows a sample setting of the experiments. Prior to the XRF and tomography measurements, X-ray transmission images (radiographs) of each keystone were taken at 7.090 and 7.135 keV, except for track 67, Namekuji (10 keV), with the same X-ray image detector used for microtomography (2000 × 1312 pixels; effective pixel size: 0.21 × 0.21 μm^2; details will be mentioned later) to do reconnaissance imaging of the whole track and captured grains along the track (Fig. 3).

XRF analysis of keystones was performed at 15 keV using a Ge-SSD detector to determine the elemental abundances along the tracks and in individual grains in track 68 Skyrocket (P1 to P4: Fig. 3b), with an exposure time of usually 2000 s and sometimes 1000 s. The beam sizes were 40 × 40 μm^2 for the individual grains (P1-P4) and from 50 × 50 μm^2 to 400 × 260 μm^2, depending on the necessary coverage for the entire track (Fig. 3). The concentrations of elements for a whole track, or a whole projectile, were calculated by adding the amounts in each measured area. As
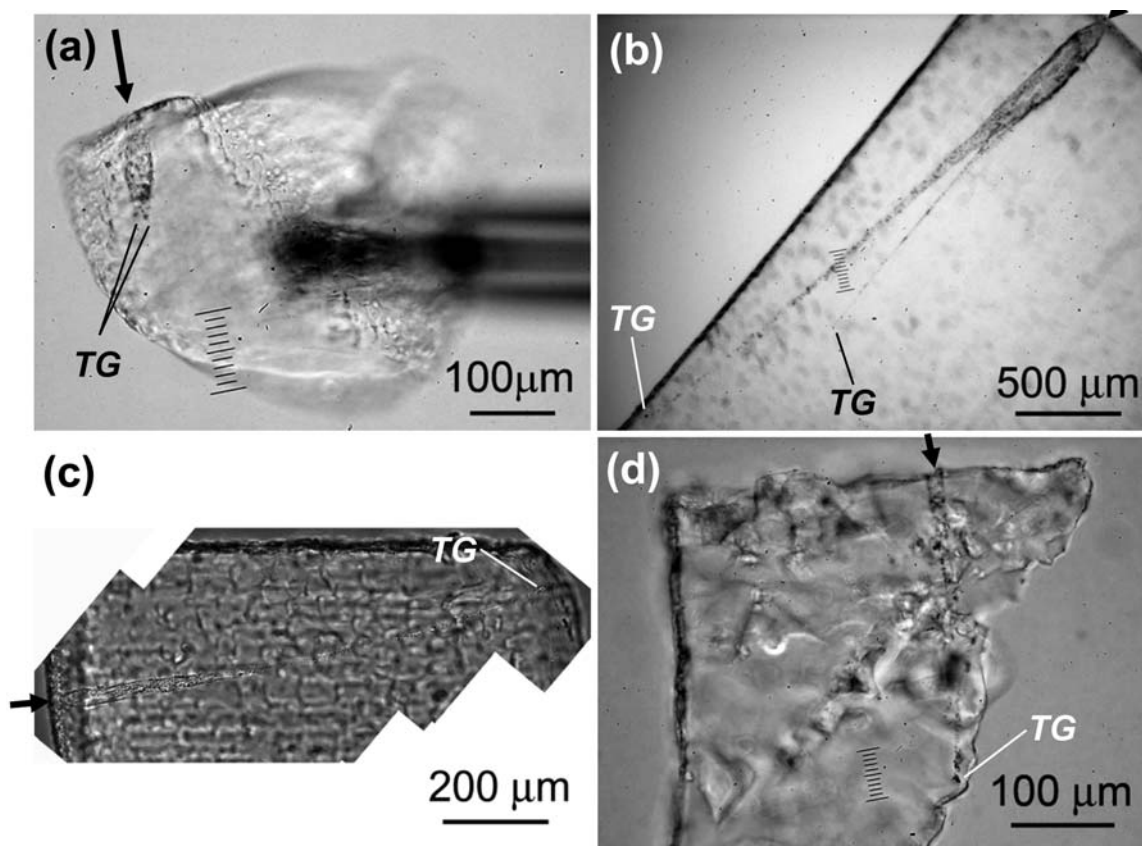
Fig. 1. Optical micrographs of the Stardust keystones used in this study. a) Track 67, Namekuji (C2126,1,67,0). b) Track 68, Skyrocket (C2126,2,68,0). c) Track 46, Gobou (C2126,4,46,0). d) Track 47 (FC13,2,47,0). Arrows indicate track entrances. Terminal grains are labeled TG. A scale used in the microscope is also imaged in (a), (b), and (c).

the measured areas overlap slightly in Skyrocket (Fig. 3b) and track 47 (Fig. 3d), the amounts should be slightly larger than the real ones.

The absolute masses of Fe and Mn were obtained for track 68, Skyrocket and track 47, while only Fe was obtained for track 67, Namekuji and track 46, Gobou. XRF counts for S, Ca, Cr, Ni, Zn, Cu, Ga, Ge, As, and Se were also obtained for Skyrocket and track 47, and Ni for Namekuji and Gobou. The integrated intensity of XRF peaks from the elements were determined by applying Gaussian fitting for peak deconvolution. For each keystone, we measured a portion of clear aerogel where no tracks and no grains are present to correct for background intensity.

The absolute mass of an element, $m(E)$ (where E = Fe or Mn), was obtained from XRF counts from a sample, $C(E)$, using the following equation;

$$m(E) = \frac{C(E)}{Y(E)ZW}[\text{g}],\qquad(1)$$

where $Y(E)$ is the sensitivity of E (cps/g) that was determined by measuring a standard sample when the distance between the XRF detector and the standard is 10 mm and the incident X-ray intensity is 10000 cps, Z is a correction factor for reducing the distance between the XRF detector and the

standard to the distance between the detector and a keystone sample, and W is a correction factor for reducing the incident X-ray intensity of 10000 cps to the intensity during the measurement of the keystone. The correction factor Z is introduced to consider absorption effects of the fluorescent X-ray during passage through the air.

The standard sample was prepared by making a glass of basalt from Ohshima Is., Japan (JB-2 in GSJ Geochemical Reference samples; Imai et al. 1995). A doubly polished thin glass film 15.9 μm thick was prepared and used. The Fe and Mn contents of the JB-2 standard were measured by an electron probe microanalyzer at Kyushu University. The results indicate that Fe = 9.2 ± 0.2 wt% and Mn = 0.16 ± 0.06 wt%, which are consistent with the literature (9.97 wt% for Fe and 0.169 wt% for Mn; Imai et al. 1995).

Th error for $m(E)$ was estimated by applying error propagation to Equation 1. Each parameter, $C(E)$, $Y(E)$, Z, and W, has its own errors that are also propagated due to several factors. For instance, an error of approximately 14% arises in the case of Fe mass (Table 2); this error is brought about by 10, 5, and 6% error in $Y(E)$, W, and Z, respectively, and the $C(E)$ error is negligible (smaller than 1%) because of high XRF counts. A relatively large error in $Y(E)$ is due to errors in estimation of JB-2's standard density.
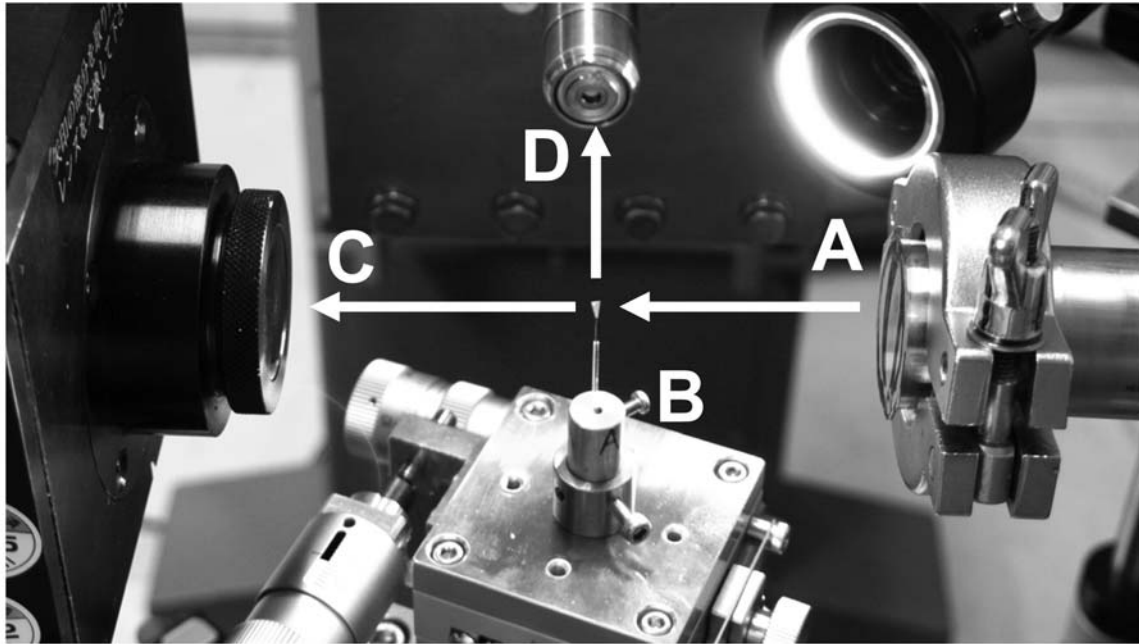
Fig. 2. Experimental setting in the present experiments. The monochromatic X-ray beam is coming from A. The sample is set on a rotation stage (B). An X-ray image detector (C) for radiography and tomography is behind the sample along the beam path and an XRF detector using a Ge-SSD (D) is perpendicular to the path. The beam monitor and the XRF detector are moved closer to the sample while imaging and measuring, respectively.

For S, Ca, Cr, Ni, Zn, Cu, Ga, Ge, As, and Se, only XRF counts were obtained, because (1) the Ca XRF peak is on the shoulder of a larger Si peak from aerogel, and thus is difficult to decompose in both the standard and the keystones, and (2) well-resolved XRF peaks of the other elements are not detected in the analysis of the standard due to low concentrations, although these peaks have been detected in keystone analysis. The XRF count $C(E)$ data make it possible to compare the element distribution within a single track (e.g., S is richer in the upper portion than the lower portion of a track), although element ratios, such as Se/S ratio differences in a track, cannot be discussed quantitatively. In this paper, only the element fraction, $X(E) = C(E)/\Sigma C(E)$, along each track was discussed for the ten elements.

Three-dimensional structures of the tracks were obtained by a projection microtomography system using X-ray attenuation developed at SPring-8 (SPμCT: Uesugi et al. 2001, 2003; Tsuchiyama et al. 2005). Images of transmitted X-ray intensities through a sample were taken at an X-ray energy of 10 keV with 1500 projections by 180 degrees of rotation. Images of incident X-ray beams without sample (white field) and the dark current of the detector system were measured before and after the CT measurement to obtain projection images of the samples. All images were obtained by an X-ray image detector, in which X-rays were transformed into visible light by a thin fluorescent screen (Lu_2SiO_5:Ce^+ single crystal plate), expanded by microscope objectives (×20 or ×50) and subsequently detected by a

cooled CCD camera (Hamamatsu Photonics, C4880-41S: 2000×1312 pixels in 2×2 binning mode) with a dynamic range of 12 bits. CT images (2000×2000 pixels in full images) were reconstructed from projection images by a convolution back-projection algorithm (Nakano et al. 2000) with Chesler's filter (Chesler and Riederer 1975) (e.g., Fig. 4). The 3-D structure was reconstructed by stacking 1312 slice images at a single CT measurement. The size of each voxel (a "volume element" or pixel in 3-D) in the 3-D images was $0.50 \times 0.50 \times 0.50 \ \mu m^3$ or $0.21 \times 0.21 \times 0.21 \ \mu m^3$ depending on the microscope objective and track size, and the effective spatial resolutions were both around 1 μm. Only tracks, not whole keystones, were imaged. CT measurements were repeated by moving the sample five times for the large tracks of Skyrocket and Gobou, and the CT slices were tiled to obtain the whole 3-D track structures. CT images became noisy when a glass fiber, which held a keystone, was present in the X-ray path for Namekuji and Gobou (e.g., Fig. 3c). However, the noise did not seriously affect image analysis. It was found by tomography that track 47 (Fig. 1d) was partly destroyed and its complete shape cannot be obtained. Thus, further analysis was not done for this track.

The 3-D CT images were analyzed using a software package for basic 3-D analysis (Slice: Nakano et al. 2006). Using this package, we performed tiling of CT slices, making cross sections in arbitrary directions (e.g., Fig. 5), binarization, making bird's eye view images for external shapes of extracted objects (e.g., Fig. 6), and calculation of
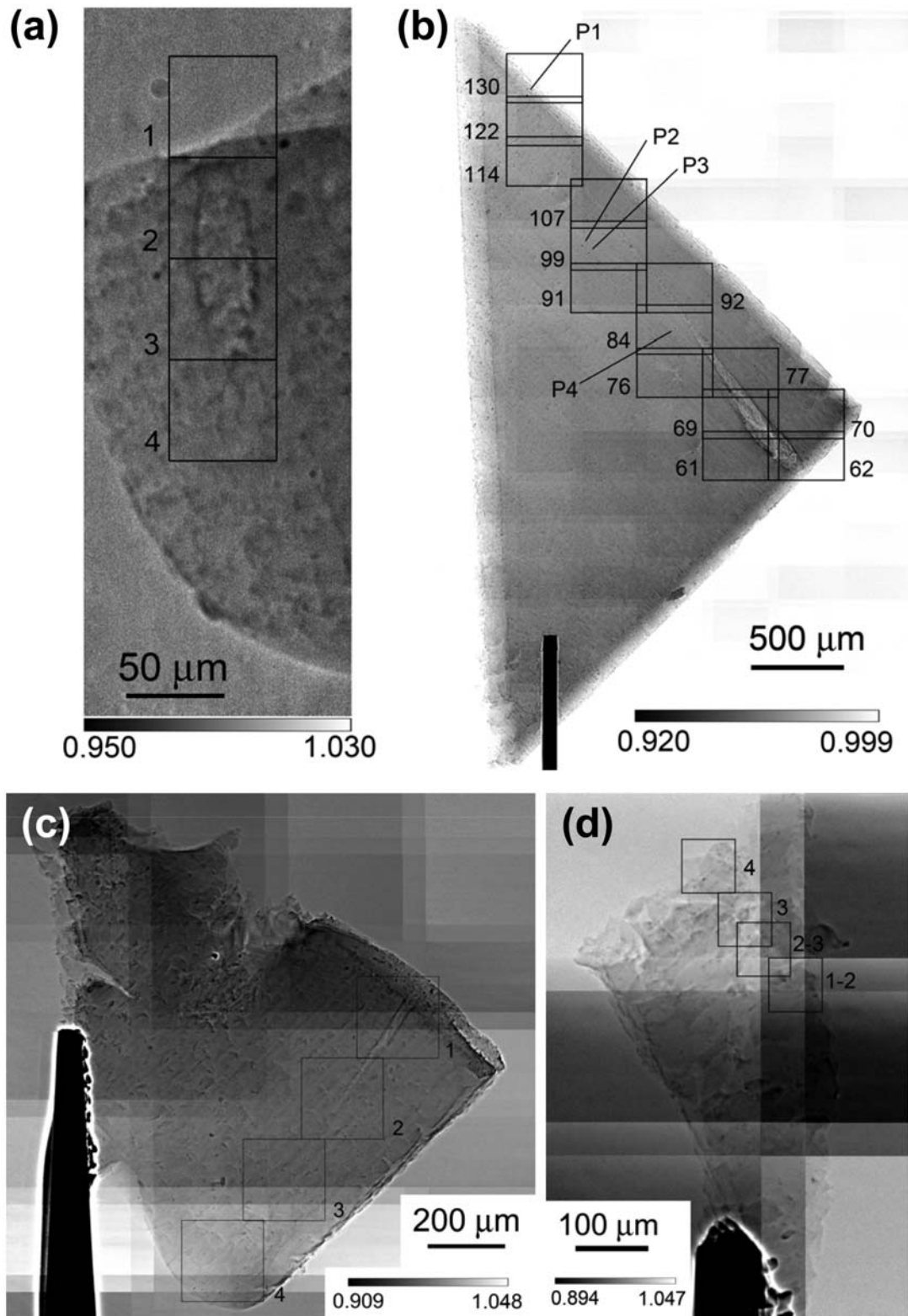
Fig. 3. X-ray radiographs (tile images) of the Stardust keystones. Transmittance, I/I_0, (I and I_0 are the intensities of transmitted and incident X-ray beams, respectively) is shown. a) Track 67, Namekuji, 10 keV. b) Track 68, Skyrocket, 7.0920 keV. c) Track 46, Gobou, 7.090 keV. d) Track 47, 7.090 keV. XRF analysis areas are superimposed as boxes. P1 to P4 in (b) label grains for XRF analysis (Table 4).

Table 2. Elemental mass distributions along impact tracks.

Track 67 (Namekuji)

Track	33W1	33W2	33W3	33W4	Total
z (μm)*	7	35	78	107	
Fe(g)	0.00E+00	0.00E+00	1.24E-12	1.56E-12	2.81E-12
±	0.00E+00	0.00E+00	1.68E-13	2.11E-13	3.78E-13

Track 46 (Gobou)

Track	47W1	47W2	47W3	47W4	Total
z (μm)[a]	114	367	643	867	
Fe(g)	5.99E-12	1.55E-12	5.99E-14	1.58E-13	7.76E-12
±	8.14E-13	2.11E-13	8.14E-15	2.14E-14	1.05E-12

Track 68 (Skyrocket)

Track + Particle	68-61	68-62	68-69	68-70	68-76	68-77	68-84,P4	68-91	68-92	68-99,P2,P3	68-106	68-107	68-114	68-122	68-130,P1	Total
z (μm)*	43	43	259	259	563	563	860	1171	1171	1480	1783	1783	2082	2380	2623	
Fe(g)	6.75E-11	7.28E-11	1.45E-10	2.14E-11	3.29E-11	8.52E-11	4.01E-11	4.19E-11	3.31E-11	1.18E-10	9.00E-13	3.06E-12	7.90E-13	2.21E-11	1.33E-10	8.17E-10
±	9.43E-12	1.02E-11	2.03E-11	2.99E-12	4.60E-12	1.19E-11	5.59E-12	5.85E-12	4.62E-12	1.64E-11	1.26E-13	4.27E-13	1.10E-13	3.08E-12	1.85E-11	1.14E-10
Mn(g)	2.62E-12	1.19E-12	1.17E-12	2.19E-12	1.72E-12	1.16E-12	1.24E-12	3.31E-13	2.56E-13	6.33E-13	1.14E-12	1.16E-12	9.03E-13	2.26E-12	5.28E-12	2.33E-11
±	4.05E-13	1.84E-13	1.81E-13	3.38E-13	2.66E-13	1.79E-13	1.91E-13	5.12E-14	3.95E-14	9.77E-14	1.76E-13	1.79E-13	1.39E-13	3.49E-13	8.16E-13	3.59E-12
(Mn/Fe)$_{CI}$	3.74	1.57	0.78	9.86	5.03	1.31	2.97	0.76	0.74	0.52	122.12	36.44	110.08	9.87	3.84	2.74
±	0.78	0.33	0.16	2.05	1.05	0.27	0.62	0.16	0.16	0.11	25.42	7.59	22.92	2.05	0.80	0.57

Track 68 (Skyrocket)

Particle	P1	P2	P3	P4	Total
z (μm)*	2670	1454	1404	813	
Fe(g)	1.33E-10	6.27E-11	4.54E-11	7.03E-12	2.48E-10
±	3.41E-11	1.10E-11	7.96E-12	1.23E-12	3.68E-11
Mn(g)	4.97E-12	1.26E-13	5.52E-14	4.75E-13	5.63E-12
±	1.16E-12	2.21E-14	9.69E-15	8.33E-14	1.16E-12
(Mn/Fe)$_{CI}$	3.61	0.19	0.12	6.50	2.19
±	1.25	0.05	0.03	1.61	0.56

Track 47

Track	32W4	32W3	32W2-3	32W1-2	Total
z (μm)*	50	143	196	257	
Fe(g)	1.82E-11	2.27E-11	8.85E-12	2.01E-11	6.99E-11
±	2.44E-12	3.03E-12	1.18E-12	2.70E-12	9.36E-12
Mn(g)	0.00E+00	9.63E-15	1.31E-14	7.11E-15	2.99E-14
±	0.00E+00	1.44E-15	1.97E-15	1.06E-15	4.47E-15
(Mn/Fe)$_{CI}$	0.000	0.041	0.143	0.034	0.041
±	0.000	0.008	0.029	0.007	0.008

[a]Mean track depth from the entrance.

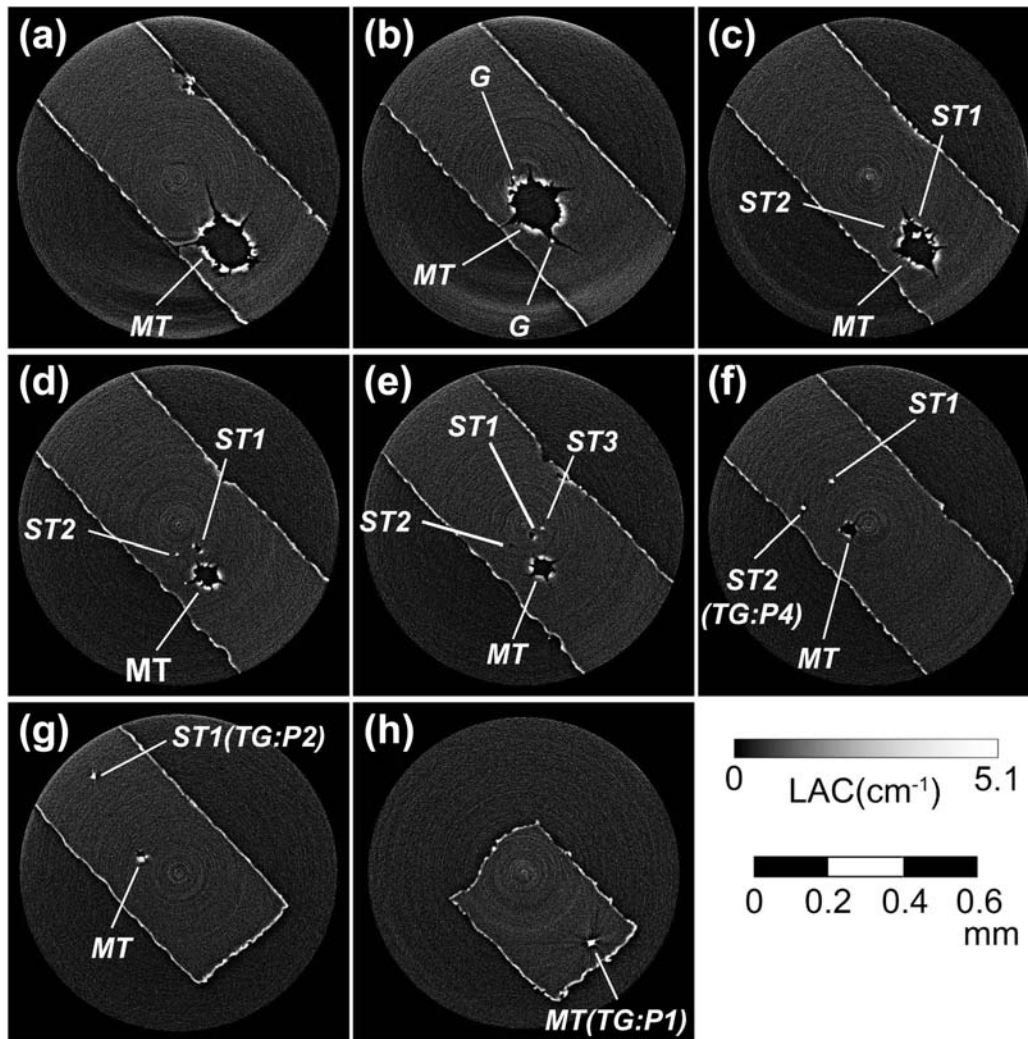Fig. 4. Examples of reconstructed CT images along track 68, Skyrocket, with voxel size of $0.50 \times 0.50 \times 0.50$ μm^3. The location of each slice is marked in Figs. 5c and 5d. We can recognize track cavities together with radial cracks, compacted aerogel, and captured grains, which are disaggregated into pieces during the capture. The captured grains, even the terminal grains, should be covered or mixed with compacted aerogel, and they are not recognized in the CT images (see text). MT: main track, G: captured grain, ST1:subtrack-1, ST2: subtrack-2, TG: terminal grain P1, P2, or P4.

areas and volumes of the tracks (Figs. 7 and 8). Cavities of the impact tracks and compacted (compressed and/or melted) aerogel grains were extracted as binary images using CT value thresholds, which were determined manually by comparing the original CT images. Grains, which may correspond to disaggregated cometary particles, were also extracted manually by considering their high CT values and textures in CT images for Skyrocket and Namekuji; bright objects are present as discrete grains on the walls or in cracks (e.g., G in Fig. 4b). The sizes of the extracted grains were overestimated because real cometary grains are covered or mixed with melted aerogel (Nakamura et al. 2008a), and they cannot be distinguished from each other by tomography alone, as will be discussed later. Size parameters of the tracks, such as length, width and volume, were determined from the binary images of track cavities.

Their uncertainties come from the CT value threshold and the voxel size. The error of the voxel size is about 1% in this study, and this causes relative errors. The error was not evaluated statistically because a sufficient number of voxel size measurements for statistical treatment was not made.

RESULTS

Three-Dimensional Structures of Tracks by Microtomography

Figure 4 shows examples of CT images of Skyrocket. While the field of view of the transmitted X-ray images does not contain whole keystone, the CT image was not greatly affected due to the low aerogel density (5 mg/cm^3 at the surface and gradually increasing toward the inside) (Yano et al.
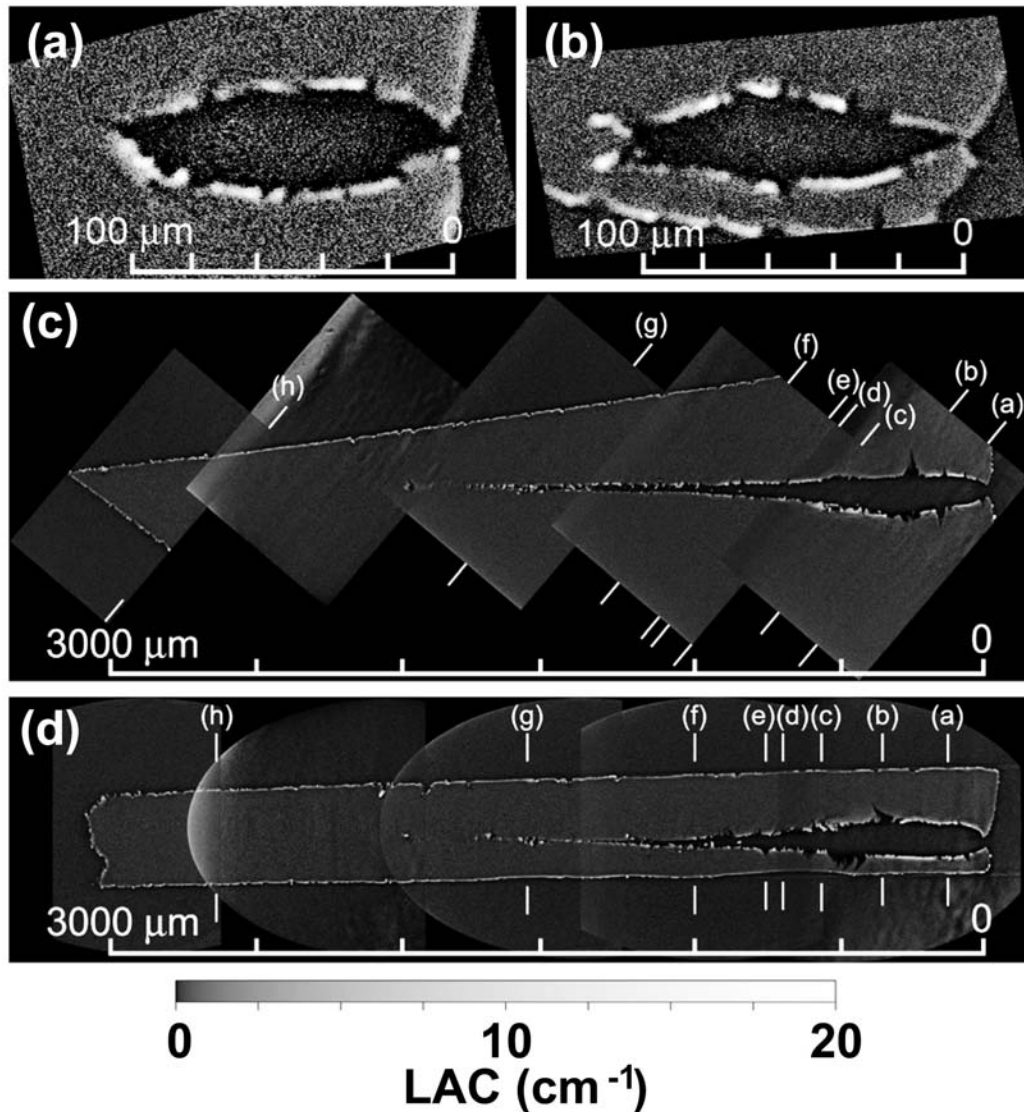
Fig. 5. CT images cut along the elongated directions of the Stardust impact tracks. A pair of images with cutting planes vertical to each other is shown. a and b) Track 67, Namekuji. c and d) Track 68, Skyrocket. (Slice positions in Fig. 4 are shown by arrows.)

2005; Ebel and Reverse 2006; Ebel et al. 2007). However, this must affect quantitative estimation of the linear attenuation coefficients (LACs) of X-rays (CT values). Therefore, quantitative discussion of the CT values is not provided. Cavities of the impact track (dark portions) and compacted aerogel grains, which were formed by compression and/or melting by a shock wave, on the track wall (bright portions) were easily recognized. Cracks that developed radially from the main track were also observed (Figs. 4a–e). The track is split into six thin tracks, including the main track. The subtracks are recognized as small holes in the CT images (ST1, 2, and 3 in Fig. 4). Discrete grains, which seem to correspond to a cometary particle disintegrated by the capture, were seen in radial cracks ("captured" grains: G in Fig. 4b) and along the track walls as well as in track terminals (TG in Figs. 4f–h). A set of bright

and dark contrasts along the aerogel surface, which is not clearly seen in Fig. 4 but is clear in the original CT images, is an artifact due to X-ray refraction at the surface (refraction contrast). Ring artifacts are also seen. However, these CT artifacts did not prevent further analysis of the 3-D CT images.

Sections nearly parallel to the elongation of the tracks were made from the 3-D CT images (Fig. 5). Each track has a narrow entrance and a bulbous portion. Thin tracks develop from the bulbs in Skyrocket (Figs. 5c–d) and Gobou (Figs. 5g–h). As the thin tracks are not strictly straight, the bulb centers, thin tracks, and terminal grains are not seen in the same image. Bird's eye views for the 3-D external shapes of the tracks, where track cavities, compacted aerogels, and "captured" grains are drawn, were made from the CT images (Fig. 6). The figures show that compacted aerogel covers
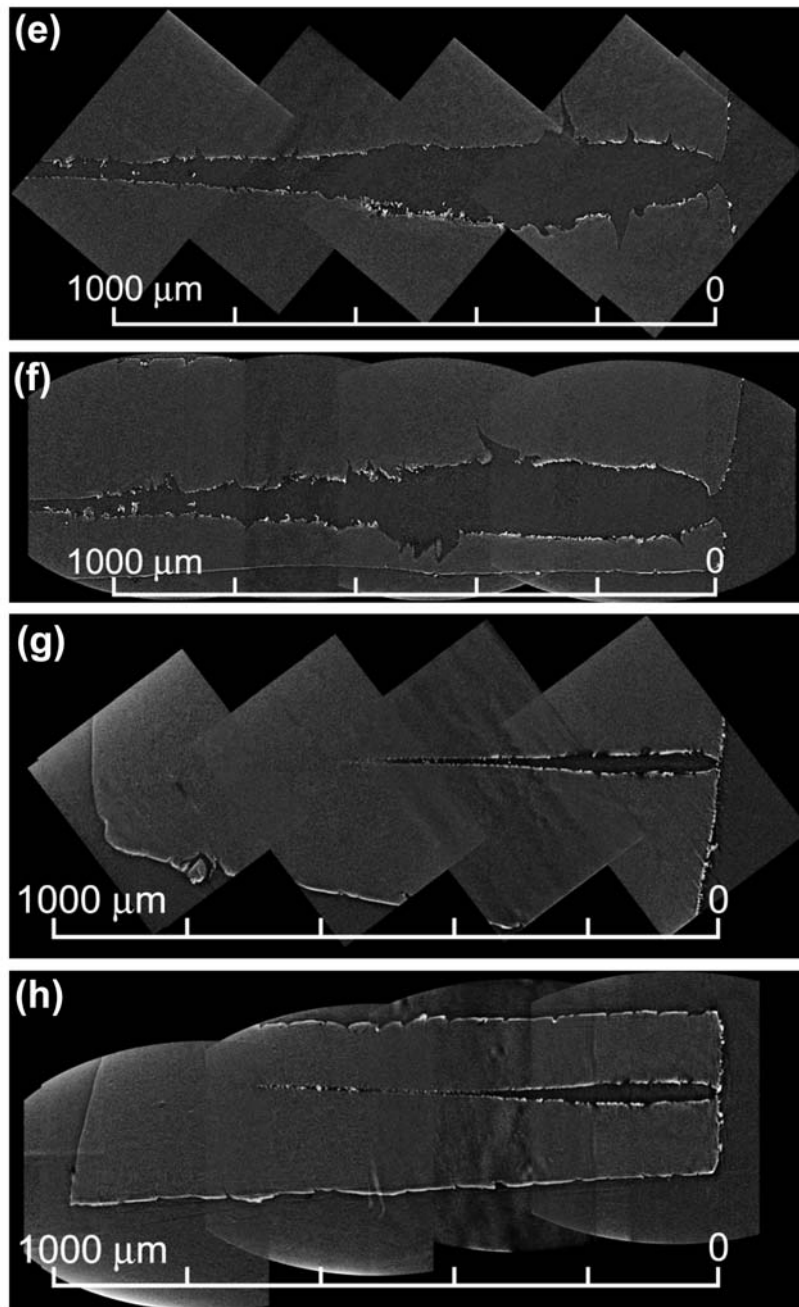
Fig. 5. *Continued*. CT images cut along the elongated directions of the Stardust impact tracks. A pair of images with cutting planes vertical to each other is shown. e and f) A bulbous portion of track 68, Skyrocket. g and h) Track 46, Gobou. The images were obtained from successive 3-D CT slices, as in Fig. 4, by image processing using Slice (Nakano et al. 2006). Five and four sets of slices imaged at a time are tiled three-dimensionally to obtain 3-D structures of tracks, 68 Skyrocket, and 46, Gobou, respectively. The images were enhanced non-linearly ($P = \mathrm{int}[255(f/20\ \mathrm{cm}^{-1})^{1/4} + 0.5]$, where P is the tone in the 8-bit images, and f is the CT value) to observe the tracks easily.

almost the whole track wall except for a thin track section near the terminus (Figs. 6b, 6e). Radial cracks are seen as planar cavities without compacted aerogel. Many "captured" grains are located along thin tracks (main and subtracks in Skyrocket [Fig. 6b]), while some are located in radial cracks (Figs. 6c–d). These grains should have entered the cracks after their opening and would have not suffered severe heating.

As CT images are digital images with a quantitative voxel size, we can make quantitative measurements for the tracks, such as track length, L_t, track volume (for the entire cavity), V_t, track entrance size, and the maximum diameter, D_m (Table 1). Comparison with the size parameters estimated from conventional measurements using an optical microscope is discussed in the Appendix. The volumes of compacted aerogels, V_{ca}, and "captured" grains, V_g, were also obtained.
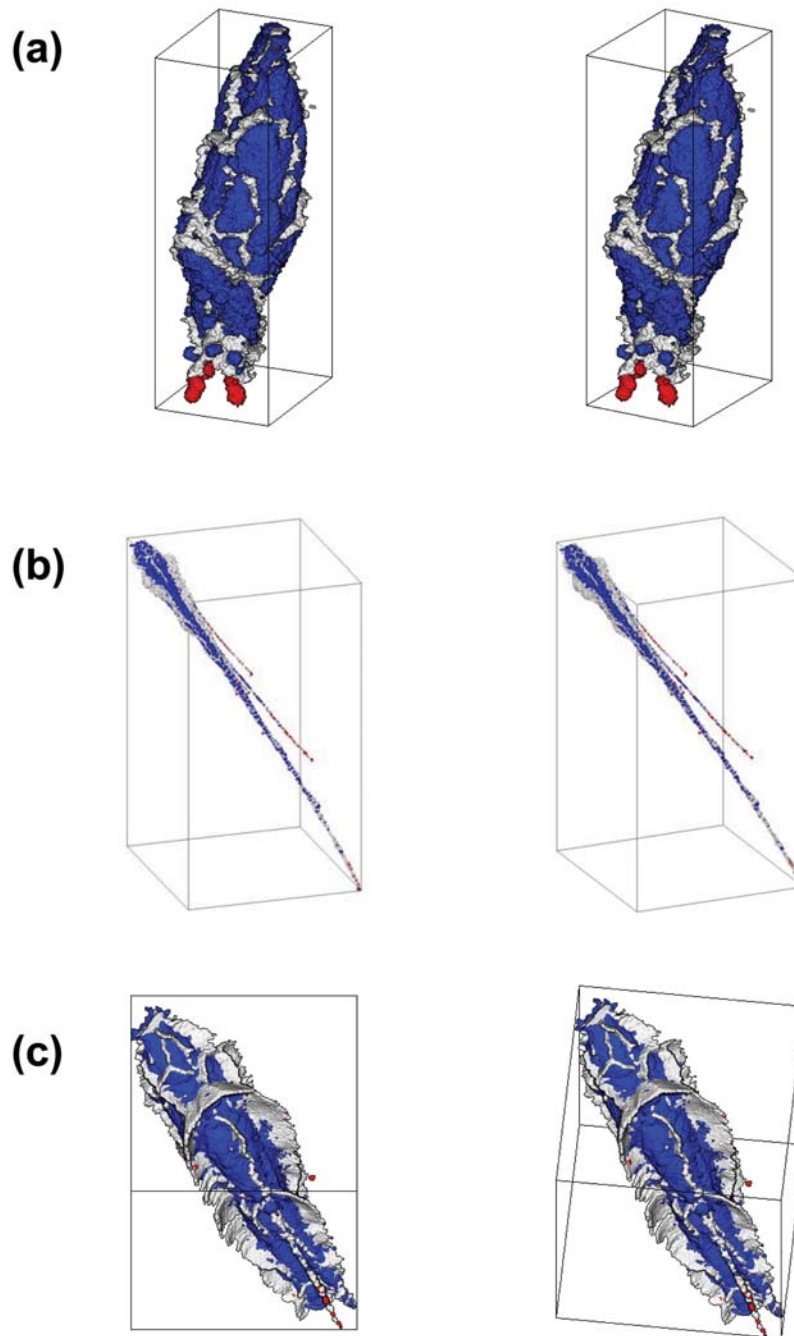
Fig. 6. Stereograms of the Stardust impact tracks. A pair of bird's eye view images is shown. a) Track 67, Namekuji. b) Track 68, Skyrocket. c) A bulbous portion of track 68, Skyrocket. Gray: track cavities (cracks on the track walls are also recognized), blue: compacted (melted and/or compressed) aerogel, and red: captured grains covered or mixed with compacted aerogel.

As we can obtain the cross-sectional areas of the track cavity, S_t, as a function of the distance from the track entrance (track depth), z, the track shape can be expressed quantitatively as the mean track radius, $r(=\sqrt{S_t/\pi})$, as a function of z (Fig. 7a). The track shapes normalized by the cube root of the track volume are also shown (Fig. 7b). The figures show that even the narrowest track of Gobou has a small bulbous portion (see

also Figs. 5g–h), where its radius is about five times larger than that of thin tracks.

Namekuji (Track 67: C2126,1,67,0)

This track is short (about 110 μm long) and has only a bulbous portion without any thin tracks from the bulb (type C of Hörz et al. 2006). Two terminal grains are recognized at the
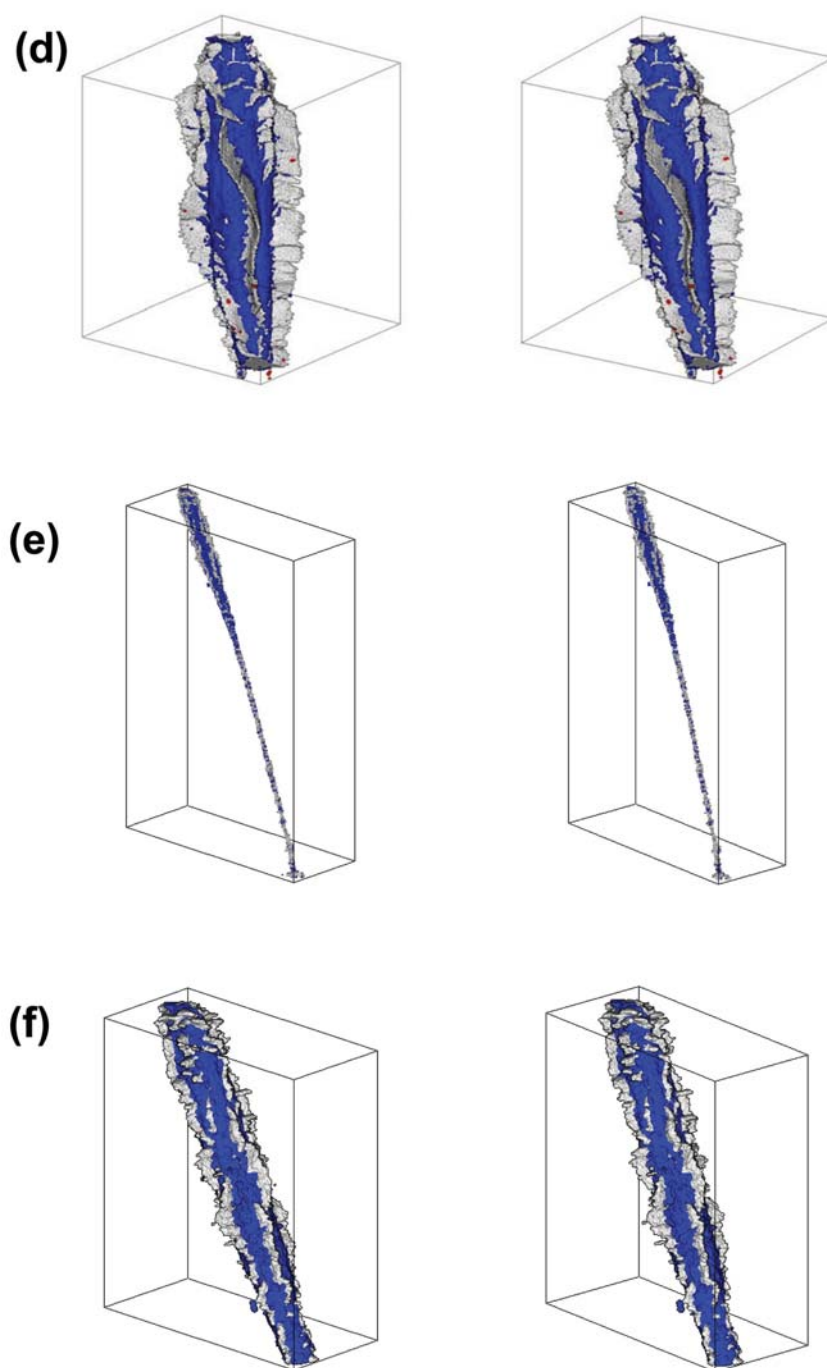
Fig. 6. *Continued*. Stereograms of the Stardust impact tracks. A pair of bird's eye view images is shown. d) A bulbous portion of track 68, Skyrocket. e) Track 46, Gobou. f) A bulbous portion of track 46, Gobou. Gray: track cavities (cracks on the track walls are also recognized), blue: compacted (melted and/or compressed) aerogel, and red: captured grains covered or mixed with compacted aerogel.

end of the bulb (Figs. 5b and 6a). The bulb does not have cylindrical symmetry and is slightly flattened (Figs. 5a, 5b). Radial cracks are irregularly developed (Fig. 6a).

Skyrocket (Track 68: C2126,2,68,0)

This track is long (about 2700 µm long) and carrot-shaped (type A of Hörz et al. 2006). The thin track is split into

five subtracks from the main track with the largest terminal grain of P1 (Figs. 4 and 6b). All the subtracks have terminal grains. The thin tracks are curved, especially the main and second tracks (Fig. 6b). The bulb wall surface is zigzag in shape (Figs. 5e, 5f), perhaps due to zones of weakness or subtle heterogeneity in the aerogel substructure. Double U-shaped radial cracks with a central small crack are observed,
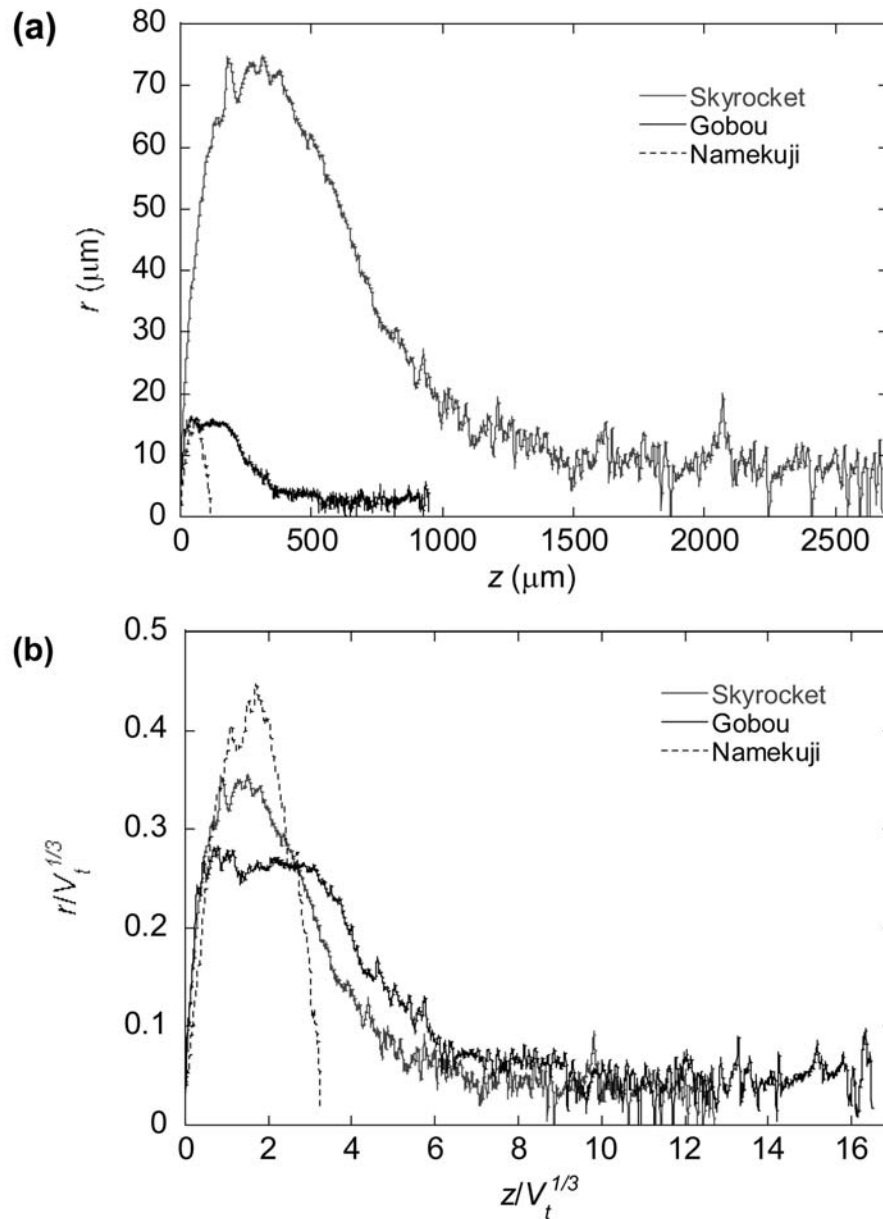
Fig. 7. Quantitative shapes of the Stardust impact tracks. a) Mean track radius, r, as a function of track depth (distance from the entrance), z. The mean radius is calculated from the cross-sectional area of the track, S, by assuming cylindrical symmetry ($S = \pi r^2$) without considering bifurcation into subtracks. b) The mean radius $vs.$ depth normalized by the cube root of the track volume, $V_t^{1/3}$.

and a subtrack has developed from the central crack (Fig. 6c). Cracks are wavy (Fig. 6d).

Gobou (Track 46: C2126,4,46,0)

This track is of medium length (about 1000 μm) and has a thin carrot shape (type A of Hörz et al. 2006). The terminal grain was not observed by tomography. This grain was present in the photograph taken at the Stardust curation office at NASA Johnson Space Center (Fig. 1c), but was lost before its arrival in our laboratory. The chipped portion of the keystone is very small if the radiograph or CT images are compared with the photograph. Thus, L_t and V_t should

be slightly smaller than the original values (Table 1). The thin track is curved (Fig. 6f) and has almost constant width (Fig. 7). Many "captured" grains are present along the thin track (Fig. 5h). Radial cracks are irregularly developed (Fig. 6f).

Elemental Compositions and Distributions in Tracks by XRF

The Fe and Mn masses of the tracks, including track 47 (FC13,2,47,0), determined by XRF are shown in Table 2. Note that the sum of the masses for track 47 and Gobou do not represent the entire bulk elemental mass of the original
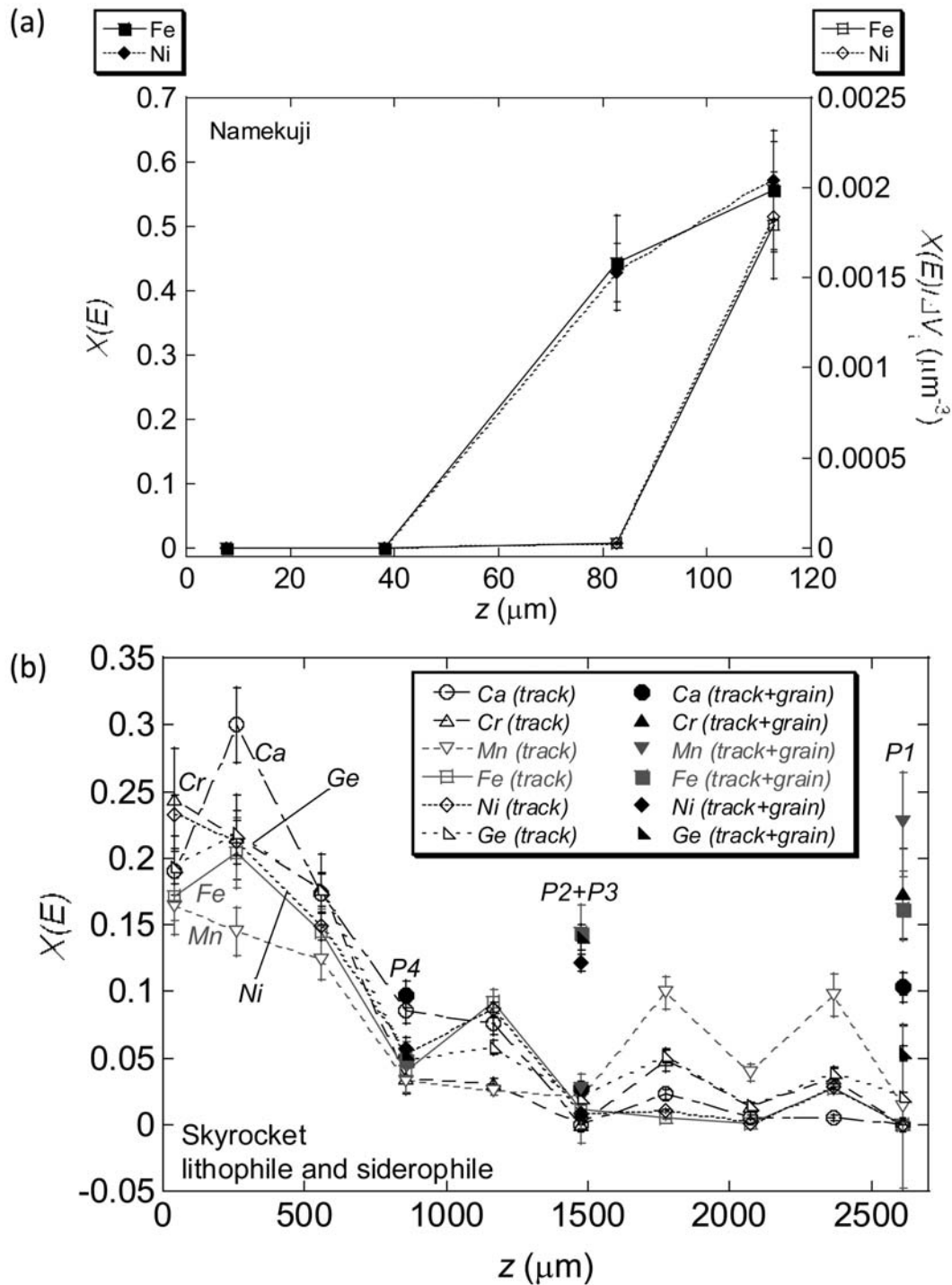
Fig. 8. Element distributions along the Stardust impact tracks. The mass fractions of an element, E, obtained by XRF for measured areas of the track, $X(E)$, and the fraction per unit track volume for each cross section, ΔV_t, are plotted against the mean track depth from the entrance, z. $X(E) = m(E)/\Sigma m(E)$ for $E =$ Fe and Mn, where $m(E)$ is the mass and $X(E) = C(E)/\Sigma C(E)$ for the other ten elements, where $C(E)$ is the XRF counts of the element. $\Sigma m(E)$ and $\Sigma C(E)$ are the sums of $m(E)$ and $C(E)$, respectively, throughout the track. For Fe, $\Sigma m(Fe)$ equals the Fe abundance of the impact particle, $m(Fe)_p$, in Table 3. a) Fe and Ni in track 67, Namekuji. b) Mass fraction of the lithophile and siderophile elements (Ca, Cr, Mn, Fe, Ni and Ge) in track 68, Skyrocket. Open symbols: the fractions in track areas without large grains (P1-P4), solid symbols: the fractions of large grains P1 at about 2700 μm (terminal grain of the main track), P2 and P3 at about 1400 μm, and P4 at about 800 μm.
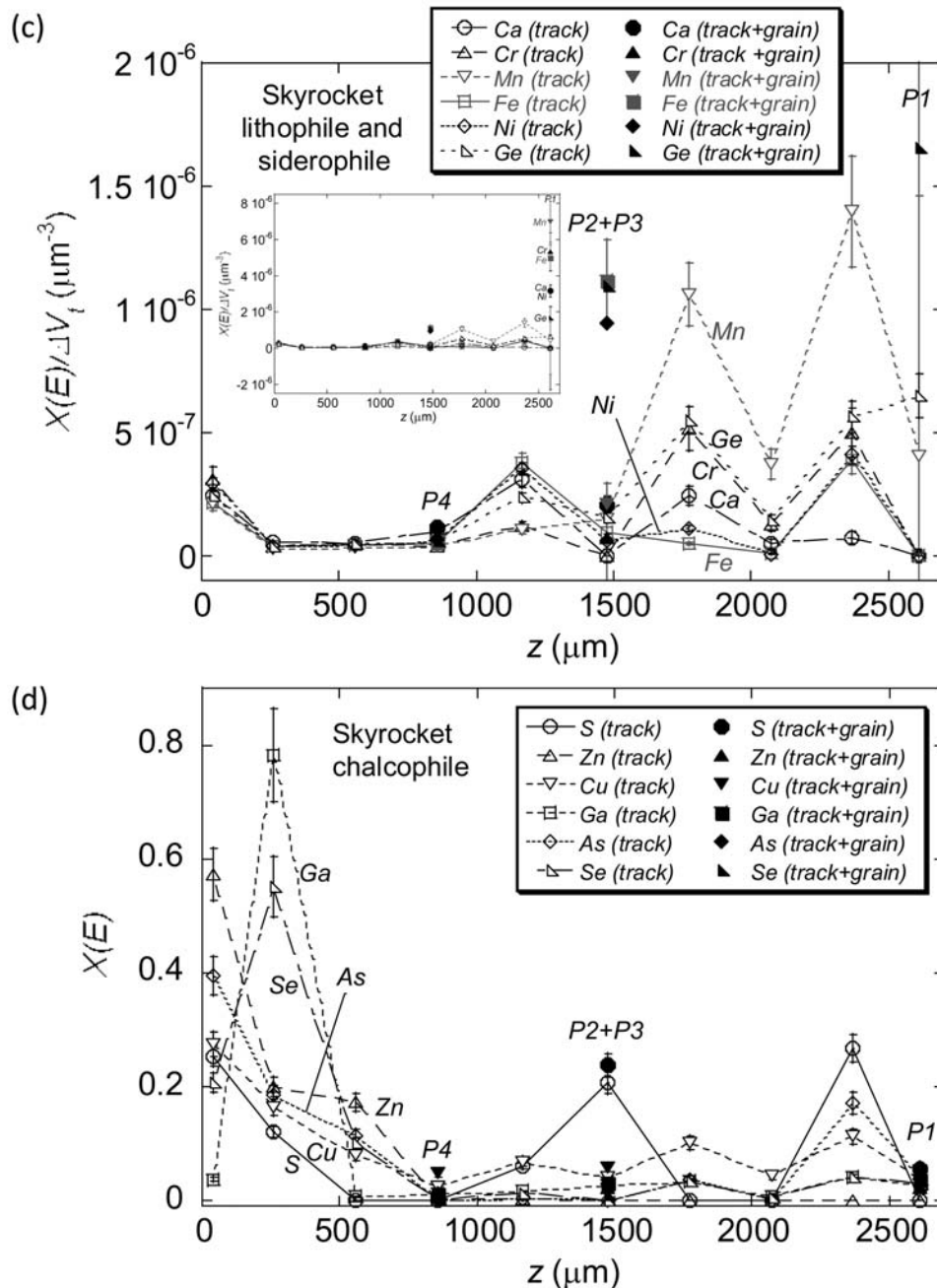
Fig. 8. *Continued*. Element distributions along the Stardust impact tracks. The mass fractions of an element, *E*, obtained by XRF for measured areas of the track, *X(E)*, and the fraction per unit track volume for each cross section, ΔV_t, are plotted against the mean track depth from the entrance, *z*. $X(E) = m(E)/\Sigma m(E)$ for E = Fe and Mn, where *m(E)* is the mass and $X(E) = C(E)/\Sigma C(E)$ for the other ten elements, where *C(E)* is the XRF counts of the element. $\Sigma m(E)$ and $\Sigma C(E)$ are the sums of *m(E)* and *C(E)*, respectively, throughout the track. For Fe, $\Sigma m(Fe)$ equals the Fe abundance of the impact particle, $m(Fe)_p$, in Table 3. c) Mass fraction per ΔV_t for the lithophile and siderophile elements in track 68, Skyrocket. d) Mass fraction of the chalcophile elements (S, Zn, Cu, Ga, As, and Se) in track 68, Skyrocket.

particles captured in the aerogel tile because track 47 was partly destroyed, and Gobou lost its terminal grain during processing. The distributions of elements along the three tracks are shown in Fig. 8, where the fraction of each element in the XRF measurement area, *X(E)*, is plotted as a function of the mean depth of the measurement area from the track entrance, *z*. *X(E)* was obtained from *m(E)* for Fe and Mn

(Equation 1, Table 2), and from *C(E)* for the other ten elements. *X(E)* divided by the track volume of the XRF measurement area, ΔV_t, is also shown (Figs. 8a, 8c, 8e, 8f). ΔV_t was obtained from tomograms integrated almost exclusively over the area where the X-ray beam hit the keystone for the XRF measurement. Normalized compositions of Mn with respect to Fe and CI are shown in
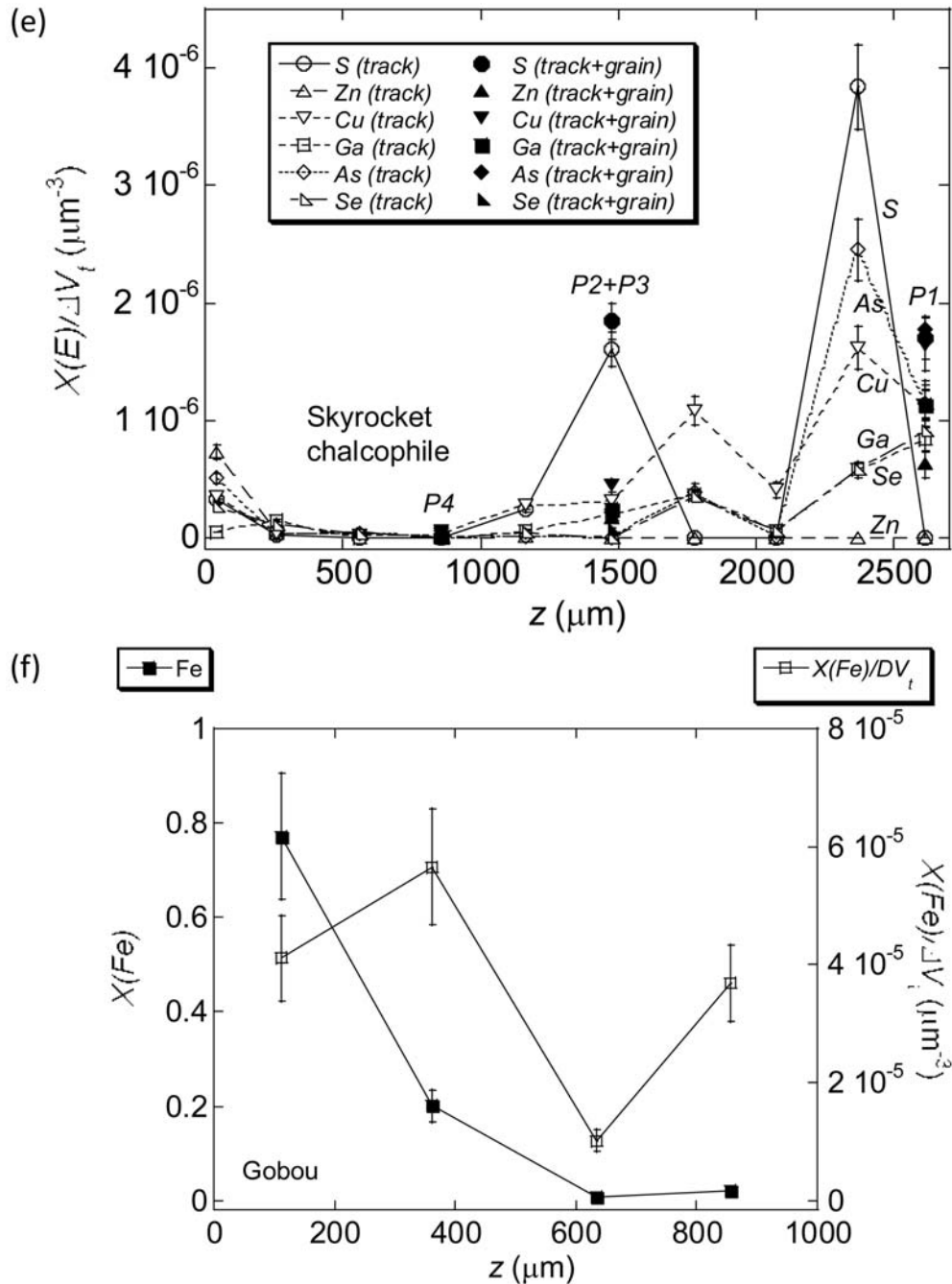
Fig. 8. *Continued*. Element distributions along the Stardust impact tracks. The mass fractions of an element, *E*, obtained by XRF for measured areas of the track, $X(E)$, and the fraction per unit track volume for each cross section, ΔV_t, are plotted against the mean track depth from the entrance, z. $X(E) = m(E)/\Sigma m(E)$ for E = Fe and Mn, where $m(E)$ is the mass and $X(E) = C(E)/\Sigma C(E)$ for the other ten elements, where $C(E)$ is the XRF counts of the element. $\Sigma m(E)$ and $\Sigma C(E)$ are the sums of $m(E)$ and $C(E)$, respectively, throughout the track. For Fe, $\Sigma m(Fe)$ equals the Fe abundance of the impact particle, $m(Fe)_p$, in Table 3. e) Mass fraction per ΔV_t for the chalcophile elements in track 68, Skyrocket. f) Fe in track 46, Gobou.

Fig. 9 for Skyrocket, together with the bulk compositions of the whole track.

Namekuji (Track 67: C2126,1,67,0)

Fe or Ni was under the detection limit near the entrance and concentrated in the bottom half of track 67 (Fig. 8a). The large elemental abundances per track volume at the track terminal correspond to the terminal grains (Fig. 6a), although the total Fe mass is much smaller than that of the large track of Skyrocket (Table 2).
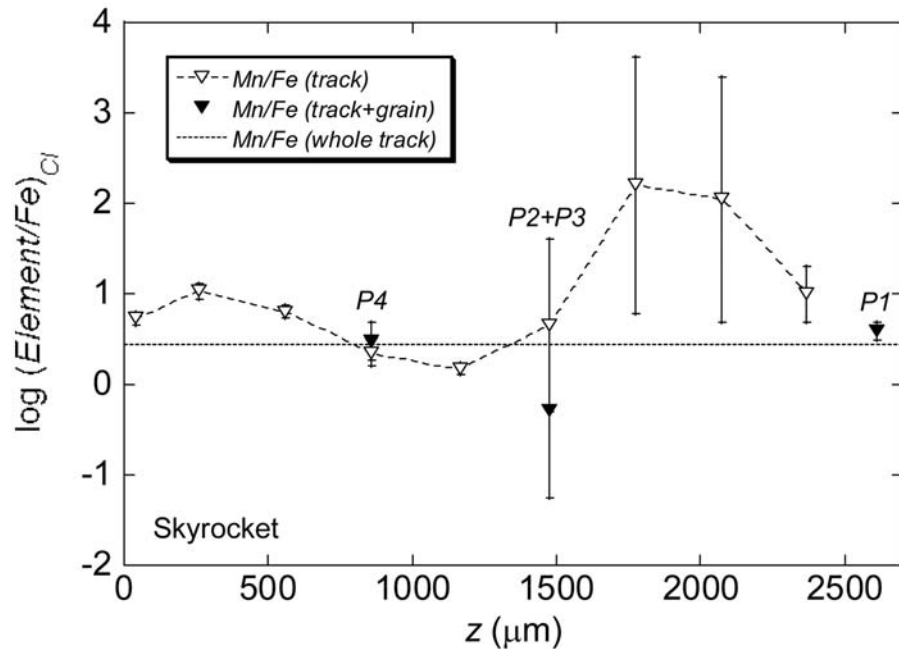
Fig. 9. Mn normalized by Fe and CI meteorites plotted against the track depth, z, for track 68, Skyrocket. Open symbols: track areas without large grains (P1-P4), solid symbols: track and individual large grains P1 at about 2700 μm (terminal grain of the main track), P2 and P3 at about 1400 μm, and P4 at about 800 μm. Dotted horizontal lines represent the bulk compositions of the track.

Skyrocket (Track 68: C2126,2,68,0)

For track 68, the elements are most enriched in the bulbous portion up to about 800 μm from the entrance, and the distribution patterns are similar to the track shape (Figs. 7a and 8b, 8d). Detailed elemental distribution patterns are different; Ca, Fe, Ge, Ga, and Se are concentrated in almost the widest portion of the track (258 μm), while Cr, Mn, Ni, S, Zn, Cu, and As are concentrated at the track entrance. On the other hand, the elemental abundances per track volume in the bulbous portion are not larger than those in thin tracks (Figs. 8c, 8e), evidence that disaggregated grains are widely distributed along thin tracks. The S content is highly variable along the track: enriched at 40, 1480, and 2380 μm and depleted at 560, 860, 1780, 2080, and 2620 μm (Figs. 8d, 8e). Some S-enriched portions of the track are not enriched in Fe (1480 and 2380 μm). Although the absorption of S fluorescence is difficult to quantify, this may suggest that S in the cometary dust particle was partly evaporated, and some recondensed along the track during particle capture, as the major phase for S is probably troilite, FeS, (or pyrrhotite, $Fe_{1-x}S$) and pentlandite, $(Fe,Ni)_9S_8$ (Zolensky et al. 2006; Nakamura et al. 2008a). The increase in Se without a corresponding increase in S at about 250 μm, and the increase in S without a corresponding increase in Se at about 1500 and 1800 μm, may suggest that S and Se are not concentrated in the same phase.

Considerable Fe is associated with three large grains (P2 and P3 at 1470 μm and P1 at the terminus) (Table 2, Fig. 8b). Fe, Cr, and Mn are concentrated, but S is not, in the terminal grain of the main track, P1, while Fe, Ni, and S are concentrated in P2 and P3 (Figs. 8b, 8d). The CI- and Fe-normalized abundance of Mn for the whole track is 2.74 ± 0.57 (Table 2). This value deviates slightly from the range of elemental composition for Wild 2 material (Flynn et al. 2006). The high Mn/Fe ratio might be ascribed to FeO-poor MnO-rich olivine and/or pyroxene (LIME) (Zolensky et al. 2006; Nakamura et al. 2008b).

Gobou (Track 46: C2126,4,46,0)

Fe in track 46 is enriched in the bulb (≲300 μm from the entrance) (Figs. 7a and 8f). However, the Fe abundances per track volume are almost the same even in the thin track area. A larger mass fraction of Fe may be present at the terminal grain, which was not measured in the present study (the grain is located outside the keystone).

DISCUSSION

Track Morphology

Hörz et al. (2006) show the relationship between the maximum diameter, D_m, and length, L_t, for different types of tracks (types A, B, and C) (Fig. S3 in their paper). The three tracks examined in this paper plot in almost the same D_m-L_t ranges as type A tracks (Skyrocket and Gobou) and type C tracks (Namekuji), while Gobou and Namekuji have slightly smaller D_m values. The Stardust track morphologies can be explained by the mixtures of two types of impacting grains:

Table 3. Total iron contents and estimated masses and sizes of projectiles in impact tracks.

Track #	Allocation	Total Fe in the track, $m(Fe)_p$ (g)	Total Fe of large grains, $\Sigma m(Fe)_g$ (g)	Fraction of large grains (wt%)	Whole particle mass*, m_p (g) × [18.67 wt%/$w(Fe)$]	Whole particle volume#, V_p (μm³) × [(1g/cm³)/ρ_p] × [18.67 wt%/$w(Fe)$]	Whole particle diameter, d_p (μm) × [(1g/cm³)/ρ_p]$^{1/3}$ × [18.67 wt%/$w(Fe)$]$^{1/3}$	$m(Fe)_p/V_t$ (g/μm³)	L_t/d_p × [ρ_p/(1 g/cm³)]$^{1/3}$ × [$w(Fe)$/18.67 wt%]$^{1/3}$	D_m/d_p × [ρ_p/(1 g/cm³)]$^{1/3}$ × [$w(Fe)$/18.67 wt%]$^{1/3}$	V_t/V_p × [ρ_p/(1 g/cm³)] × [$w(Fe)$/18.67 wt%]	Whole particle diameter, $d_{p,calc}$ (μm)[†]
Track 67	C2126,1,67,0 (Namekuji)	2.81(.38)E-12	n.d.	n.d.	1.50(.20)E-11	15.0(2.1)	3.06(.14)	6.17(.83)E-17	37.2(1.7)	10.4(.5)	3.04(.41)E+03	5.1(3.9)
Track 68	C2126,2,68,0 (Skyrocket)	8.17(1.14)E-10	2.48(37)E-10	30.3(6.2)	4.38(.61)E-09	4380(610)	20.3(.9)	8.91(1.24)E-17	131(6)	7.31(.34)	2.09(29)E+03	13.9(4.5)
Track 46	C2126,4,46,0 (Gobou)	>7.76(1.05)E-12	n.d.	n.d.	>4.16(.56)E-12	>41.6(5.6)	>4.30(.19)	>3.96(.54)E-17	<222(10)	<7.58(.65)	<4.72(.64)E+03	5.2(3.9)

*Estimated by the CI composition: $w(Fe)$ = 18.67 wt% (Dodd 1981).
#Estimated by assuming the impact grain density, ρ, of 1 g/cm³.
†Calculated based on Equation 8 of Burchell et al. (2008) using D_m (Table 1).
n.d.: not determined.
Errors are shown in parentheses.

Table 4. Volumes of grains in Skyrocket estimated from CT and XRF.

Grain#	Volume by CT, V_g (μm³)	Fe mass by XRF, $m(Fe)_g$ (g)	Total mass*, m_g (g) × [18.67 wt%/$w(Fe)$]	Volume from mg, V_g' (μm³) × [(1 g/cm³)/ρ_g] × [18.67 wt%/$w(Fe)$]	V_g/V_g' × [ρ_g/(1 g/cm³)] × [$w(Fe)$/18.67 wt%]
P1	2693	1.33(34)E-10	7.10(1.83)E-10	710(183)	3.2(8)
P2	1184	6.27(1.10)E-11	3.36(59)E-10	336(59)	2.9(5)
P3	1062	4.54(80)E-11	2.43(43)E-10	243(43)	3.6(6)
P4	945	7.03(1.23)E-12	3.77(66)E-11	37.7(6.6)	21(4)

*Estimated by the CI composition: $w(Fe)$ = 18.67 wt% (Dodd 1981).
Errors are shown in parentheses.

fragile materials of very fine grain, which form bulbous tracks, and less fragile and relatively coarse grains, which form thin tracks with large terminal particles (Brownlee et al. 2006; Hörz et al. 2006; Zolensky et al. 2006). The present results on the three-dimensional structures of the tracks are also consistent with this explanation. Based on the Fe distribution in Skyrocket, about 30(±6)% of Fe is present in the four largest grains (P1-P4) (Table 3), and most of the rest are present in the track walls or cracks. This indicates that more than half the Fe was removed from an incoming cometary particle during deceleration in the aerogel and is consistent with results from other track analyses (Flynn et al. 2006).

The thin tracks of Skyrocket and Gobou are curved (Figs. 6b, 6e). Curved tracks are not rare (Hörz et al. 2006). They might be formed by high-speed spinning of projectiles (the so-called Magnus effect; Magnus 1853) in the aerogel, and the spinning might occur when an irregularly shaped projectile collide with the flat aerogel surface at hypervelocity, although we cannot exclude the possibility that the curved tracks are merely due to heterogeneity in the aerogel structure.

Estimation of Impact Particle Mass and Size

We may estimate the whole mass of the impact particle, m_p, for each track from the total Fe mass in the track, $m(Fe)_p$, by assuming that the Fe content of each impactor, $w(Fe)$, matches that of CI meteorites (18.67 wt%; Dodd 1981). Then, the total particle volume, V_p, and its spherical diameter, d_p, can be estimated by assuming the particle density, ρ_p,

$$d_p = \left[\frac{6m(Fe)_p}{\pi w(Fe)\rho_p}\right]^{1/3}. \tag{2}$$

The results are shown in Table 3. If the particle volume is compared with the track volume, V_t, $V_t/V_p \sim 3 \times 10^3 \times [\rho_p/(1\ \text{g/cm}^3)] \times [w(Fe)/18.67\ \text{wt\%}]$. Flynn and Sutton (1991) measured the densities of porous chondritic IDPs, and reported a mean density of 0.6 g/cm^3. However, the Wild 2 grains do not necessarily have to be similar to the porous IDPs. Thus, we assumed ρ_p of 1 g/cm^3 here for simplicity.

If the track volume, V_t, is proportional to the kinetic energy of an impact particle, $E_{kin} = 1/2 m_p v_p^2$ (Kadono 1999), V_t is proportional to the particle mass, m_p, particularly for Stardust samples where the impact velocity, v_p, is almost constant (6.1 km/s; Brownlee et al. 2006). If this is the case, the ratio of the Fe content to the track volume, $m(Fe)_p/V_t$, should be proportional to the Fe content of the particles, $m(Fe)_p/m_p$, and thus the $m(Fe)_p/V_t$ ratio should be the same for the same Fe content, such as CI composition. In fact, the $m(Fe)_p/V_t$ ratios are similar for Namekuji and Skyrocket (Table 3). If the missing terminal grain is taken into consideration, the ratio for Gobou may have a similar value;

about half of $m(Fe)_p$ should be included in the missing grain. Mineralogical studies on Wild 2 grains extracted from impact tracks showed that some are dominated by Fe sulfides, which have higher Fe contents than CI, low Fe olivine and pyroxenes, and Fe-poor Ca-Al-rich particles (Zolensky et al. 2006). Moreover, the chemical compositions of impactors that made individual tracks and craters on Al foils are not homogeneous (Flynn et al. 2006; Keaseky et al. 2008). However, the similar $m(Fe)_p/V_t$ ratios suggest that the Fe contents of the impactors for the present three tracks are almost the same, and might correspond to those of CI composition. The estimated impactor particle diameter, d_p, is also similar to the estimation using experiments from the track maximum width, D_m (Burchell et al. 2008) (Table 3). We cannot exclude the possibility that the three impactors have similar Fe contents by chance.

The volumes of individual grains can be also estimated from the tomography (grains in red in Fig. 6). The total volume of the large grains, ΣV_g, in Skyrocket is $3.80 \times 10^4\ \mu\text{m}^3$ (Table 1). This is significantly larger than the particle volume estimated from the Fe content ($V_p \sim 4.4(6) \times 10^3\ \mu\text{m}^3 \times [(1\ \text{g/cm}^3)/\rho_p] \times [18.67\ \text{wt\%}/w(Fe)]$: Table 3). The volumes of the four large individual grains in Skyrocket (P1-P4 in Fig. 3b) were also examined (Table 4). Each grain volume estimated from tomography, V_g, is also larger than those inferred from the Fe content, V_g', by ~3× for P1-P3 and ~20× for P4. SR-based XRD study for individual grains extracted from other Stardust tracks shows that the grains are divided into two types, crystalline and amorphous-rich (Nakamura et al. 2008a). SR-based microtomography with ~100 nm resolution for the crystalline grains showed that they are always covered with compacted aerogel (Nakamura et al. 2008a). The amorphous-rich grains are porous, and a small amount of very fine minerals are distributed in amorphous materials, likely mixtures of very fine fragile materials of the original cometary dust with large volumes of melted aerogel at a submicron scale (Nakamura et al. 2008a; Rietmeijer et al. 2008). In fact, a fine-grained chondritic composition material without disaggregation was found in track 57 (Fibo) (Brownlee et al. 2006). We cannot distinguish cometary grains from compacted aerogel accurately by tomography, and so the particle volumes were overestimated from the tomography. The relatively small V_g/V_g' ratios of P1-P3 suggest crystalline types covered with compacted aerogel, while the large V_g/V_g' ratio of P4 may suggest an amorphous-rich type mixed with large volumes of aerogel. Based on elemental abundances, P1 might be mainly composed of metal and Mn-rich olivine and/or pyroxene, and P2 and P3 might be composed of Fe sulfide(s). The terminal grains of Namekuji may be the amorphous-rich type because of their low Fe content compared with their large volume. The track shape of Gobou strongly suggests that its missing terminal grain is the crystalline type.
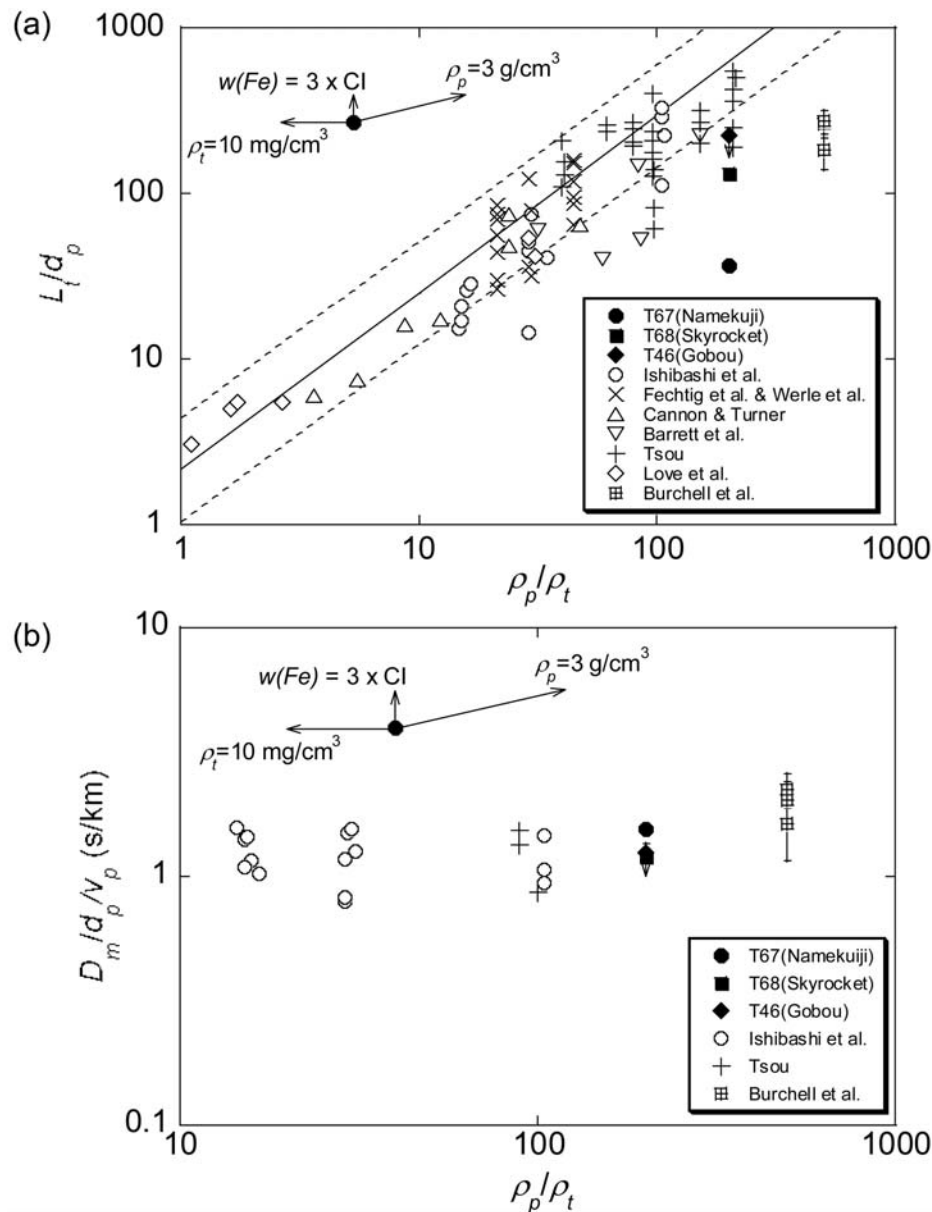
Fig. 10. Comparison of the Stardust track shapes with those in hypervelocity impact experiments. a) Track length, L_t, normalized by projectile size, d_p, plotted against the density ratio of projectiles to target, ρ_p/ρ_t. b) Normalized maximum track width, D_m/d_p, divided by impact velocity, v_p, plotted against ρ_p/ρ_t. Experimental data of Ishibashi et al. (1990) (nylon projectiles into foamed polystyrene targets), Fechtig et al. (1980) and Werle et al. (1981) (steel projectiles into porous alumina target), Cannon and Turner (1967) (nylon, magnesium, aluminum and steel projectiles into polyurethane foam targets), Barrett et al. (1992) (olivine projectiles into aerogel targets), Tsou (1990) (aluminum projectiles into polystyrene, polyimide, polyethylene, and polyacrylonitrile form targets), and Love et al. (1993) (soda lime glass projectiles into sintered soda lime glass beads target) were compiled by Kadono et al. (1999). Experiments of Burchell et al. (2008) used soda lime glass projectiles into Stardust-grade aerogel targets at 5.8–6.1 km/s. Possible deviations of the projectile density, ρ_p, from 1 to 3 g/cm^3 for the Stardust tracks, those of the Fe content in the projectile, $w(Fe)$, from CI composition (18.67 wt%) to $3 \times$ CI (56.01 wt%) for the Stardust tracks and those of the target density, ρ_t, from 5 to 10 g/cm^3 for the Stardust and Burchell et al. tracks are shown by right-upward, upward, and horizontal leftward arrows, respectively.

Comparison with Previous Studies for Estimating Track Formation Conditions

Dominguez et al. (2004) proposed a model for track formation in which aerogel is crushed due to the shock wave of the impact without any projectile fragmentation and evaporation. In this simple model, the track width decreases monotonically toward the terminal. The track lengths, L_t, for the three Stardust tracks were calculated from this model (Table 1) with an assumed average aerogel density (5 mg/cm^3) and the estimated projectile sizes, d_p, and density, ρ_p ($L_{t,calc}$ in Table 1). They are sufficiently larger than the real
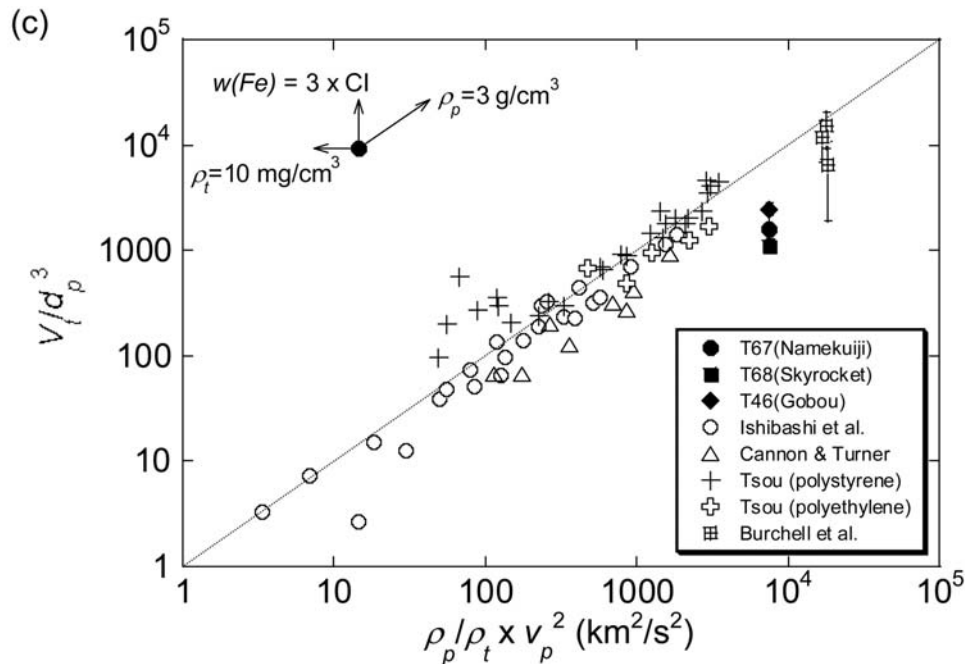
Fig. 10. *Continued*. Comparison of the Stardust track shapes with those in hypervelocity impact experiments. c) Normalized track volume, V_t/d_p^3, plotted against a parameter related to the impact kinetic energy, $(\rho_p/\rho_t)v_p$. Experimental data of Ishibashi et al. (1990) (nylon projectiles into foamed polystyrene targets), Fechtig et al. (1980) and Werle et al. (1981) (steel projectiles into porous alumina target), Cannon and Turner (1967) (nylon, magnesium, aluminum and steel projectiles into polyurethane foam targets), Barrett et al. (1992) (olivine projectiles into aerogel targets), Tsou (1990) (aluminum projectiles into polystyrene, polyimide, polyethylene, and polyacrylonitrile form targets), and Love et al. (1993) (soda lime glass projectiles into sintered soda lime glass beads target) were compiled by Kadono et al. (1999). Experiments of Burchell et al. (2008) used soda lime glass projectiles into Stardust-grade aerogel targets at 5.8–6.1 km/s. Possible deviations of the projectile density, ρ_p, from 1 to 3 g/cm^3 for the Stardust tracks, those of the Fe content in the projectile, $w(Fe)$, from CI composition (18.67 wt%) to $3 \times$ CI (56.01 wt%) for the Stardust tracks and those of the target density, ρ_t, from 5 to 10 g/cm^3 for the Stardust and Burcell et al. tracks are shown by right-upward, upward, and horizontal leftward arrows, respectively.

track lengths, L_t, even if the density gradient of the aerogel (from 5 to 50 mg/cm^3) is considered. The difference is due to the projectile fragmentation, evaporation and reaction with aerogels inferred from Stardust tracks (Rietmeijer et al. 2008; Nakamura et al. 2008a).

Kadono (1999) compiled previous hypervelocity impact experimental data, using mainly polystyrene targets, by using track shape parameters normalized by impact particle properties, such as the normalized track length, L_t/d_p, and impact conditions, such as the impact velocity, v_p, and aerogel density, ρ_t. As the projectile diameter, d_p, was estimated in this study, the present results for the Stardust tracks can be compared with the previous experiments together with experiments using spherical glass projectiles and a Stardust-grade silica aerogel target (Burchell et al. 2008).

In Fig. 10a, the normalized track lengths are plotted against the ratios between projectile and target densities, ρ_p/ρ_t. The data with $\rho_p = 1$ g/cm^3 and $\rho_t = 5$ mg/cm^3 are plotted for the present Stardust tracks. In this figure, a leftward horizontal arrow shows possible deviation of ρ_t from 5 to 10 mg/cm^3 by considering the density gradient near the aerogel surface, a right-upward arrow that of ρ_p from 1 to 3 g/cm^3 (d_p is also dependent on ρ_p in Equation 2), and an upward

arrow that of $w(Fe)$ from CI composition (18.67 wt%) to $3 \times$ CI. A downward arrow for Gobou shows the correction for $m(Fe)_p$ by considering the missing terminal grain in Equation 2. Possible deviations of ρ_t (leftward arrow) also exit for the data of Burchell et al. The value of L_t/d_p for the type A tracks (Skyrocket and Gobou) and Burchell et al.'s data, where silica aerogel was used as targets, are slightly smaller than the fitting line for polystyrene or polyethylene targets (Kadono 1999). This is consistent if we consider the effect of the impact velocity, v_p, on L_t/d_p, where L_t/d_p increases first and then decreases with increase of v_p (the maximum is at about $v_p = 2$ km/s for $\rho_t = 74$ mg/cm^3 in Fig. 2a of Kadono 1999). The small value of L_t/d_p for the type C track (Namekuji) is due to energy dissipation by disaggregation of very fine-grained dust particles.

The normalized maximum track width, D_m/d_p, divided by v_p is plotted against ρ_p/ρ_t in Fig. 10b. D_m/d_p is almost proportional to v_p for $v_p \gtrsim 1.5$ km/s irrespective of ρ_p/ρ_t (Kadono 1999). The Stardust and Burchell et al. data are almost consistent with this trend. This indicates that d_p can be estimated from D_m, as Burchell et al. did.

Figure 10c shows the normalized track volume, V_t/d_p^3, plotted against a parameter related to the impact kinetic energy,

$\rho_p/\rho_t v_p^2$. The Stardust and Burchell et al. data are almost consistent with the previous data, although the V_t/d_p^3 values for the Stardust tracks are slightly smaller than the trend. This may be due to the possibility that V_t measured using optical microscopes is overestimated (see the Appendix).

The tomography measurement gives quantitative and detailed data on the track morphologies (e.g., Fig. 7) and the distribution of impact particles (Fig. 6). This illustrates the possibility that more details about the physical conditions of the impact could be obtained by further modeling and experiments together with the present data. This will, together with XRF data, allow reconsideration in detail of the texture, crystallinity, and chemical composition of the original dust of comet Wild 2.

Editorial Handling—Dr. Scott Sandford

REFERENCES

Anders E. and Grevesse N. 1989. Abundances of the elements—meteoritic and solar. *Geochimica et Cosmochimica Acta* 53: 1711–1716.

Barrett R. A., Zolensky M. E., Hörz F., Lindstrom D. J., and Gibson E. K. 1992. Suitability of silica aerogel as a capture medium for interplanetary dust. Proceedings, 22nd Lunar and Planetary Science Conference. pp. 203–212.

Brownlee D., Tsou P., Aleon J., Alexander C. M. O'D. and 181 additional authors. 2006. Comet 81P/Wild 2 under a microscope. *Science* 314:1711–1716.

Burchell M. J., Fairey S. A. J., Wozniakiewicz P., Brownlee D., Hörz F., Kearsley A. T., See T. H., Tsou P., Westphal A., Green S. F., Trigo-Rodriguez J. M., and Dominguez G. 2008. Characteristics of cometary dust tracks in Stardust aerogel and laboratory calibrations. *Meteoritics & Planetary Sciences* 43:23–40.

Cannon E. T. and Turner G. H. 1967. Cratering in low-density targets. NASA CR-798.

Chesler D. A. and Riederer S. J. 1975. Ripple suppression during reconstruction in transverse tomography. *Physical and Medical Science* 20:632–636.

Ciesla F. J. 2007. Outward transport of high-temperature materials around the midplane of the solar nebula. *Science* 318:613–615.

Dodd R. T. 1981. *Meteorites: A petrologic-chemical synthesis.* Cambridge: Cambridge University Press. 368 p.

Danilyuka A. F., Kirillov V. L., Savelieva M. D., Bobrovnikov V. S., Buzykaev A. R., Kravchenko E. A., Lavrov A.V., and Onuchin A. P. 2002. Recent results on aerogel development for use in Cherenkov counters. *Nuclear Instruments and Methods in Physics Research A* 494:419–494.

Dominguez G., Westphal A. J., Jones S. M., and Phillips M. L. F. 2004. Energy loss and impact cratering in aerogels: Theory and experiment. *Icarus* 172:613–614.

Ebel D. S. and Rivers M. L. 2006. High spatial resolution 3D local lambda-tomography of particle tracks and fragmentation in whole aerogel tiles (abstract). 2006 Meeting of SPIE.

Ebel D. S., Mey J. L., and Rivers M. L. 2007. Nondestructive laser confocal scanning microscopy and synchrotron microtomography of single Stardust and analog tracks in aerogel keystones. 38th Lunar Planetary Science Conference. Abstract #1977.

Fechtig H., Nagel K., and Pailer N. 1980.3 Collisional processes of iron and steel projectiles on targets of different densities. In *Solid particles in the solar system*, edited by Halliday I. and McIntosh B. A. Proceedings, IAU Symposium 90. Dordrecht: Kluwer. pp. 357–364.

Flynn G. F., Bleuet P., Borg J., Bradley J. P., and 75 additional authors. 2006. Elemental compositions of comet 81P/Wild 2 samples collected by Stardust. *Science* 314:1731–1735.

Flynn G. J. and Sutton S. R. 1991. Cosmic dust particle densities: evidence for two populations of stony micrometeorites. Proceedings, 21st Lunar and Planetary Science Conference. pp. 541–547.

Greenberg J. M. and Li A. 1999. Morphological structure and chemical composition of cometary nuclei and dust. S*pace Science Reviews* 90:149–161.

Hörz F., Bastien R., Borg J., Bradley J. P. and 40 additional authors. 2006. Impact features on Stardust: implications for comet 81P/Wild 2 dust. *Science* 314:1716–1719.

Imai N., Terashima S., Ihoh S., and Ando A. 1995. 1994 Compilation of analytical data for minor and trace elements in seventeen GSJ geochemical reference samples, "igneous rock series." *Geostandards Newsletter* 19:135–213.

Ishibashi T., Fujiwara A., and Fujii N. 1990. Penetration of hypervelocity projectile into foamed polystyrene. *Japanese Journal of Applied Physics* 29:2543–2549.

Ishii H. A., Bradley J. P., Dai Z. R., Chi M., Kearsley A. T., Burchell M. J., Browning N. D., and Molster F. 2008. Comparison of comet 81P/Wild 2 dust with interplanetary dust from comets. *Science* 319:447–450.

Kadono T. 1999. Hypervelocity impact into low density material and cometary outburst. *Planetary and Space Science* 47:305–318.

Kearsley A. T., Borg J., Graham G. A., Burchell M. J., Cole M. J., Leroux H., Bridges J. C., Hörz F., Wozniakiewicz P. J., Bland P. A., Bradley J. P., Dai Z. R., Teslich N., See T., Hoppe P., Heck P. R., Huth J., Stadermann F. J., Floss C., Marhas K., Stephan T., and Leitner J. Dust from comet Wild 2: Interpreting particle size, shape, structure, and composition from impact features on the Stardust aluminum foils. 2008. *Meteoritics & Planetary Sciences* 43:41–73.

Keller L. P., Bajt S., Baratta G. A., Borg J. and 29 additional authors. 2006. Infrared spectroscopy of comet 81P/Wild 2 samples returned by Stardust. *Science* 314:1728–1731.

Love S. G., Hörz F., and Brownlee D. E. 1993. Target porosity effects in impact cratering and collisional disruption. *Icarus* 86:129–151.

Magnus G. 1853. Uber die Abweichung der Gesechesse. *Pogendorf's Annalen der Physik und Chemie* 88:1–14.

McKeegan K. D., Aleon J., Bradley J., Brownlee D. and 43 additional authors. 2006. Isotopic compositions of cometary matter returned by Stardust. *Science* 314:1724–1728.

Nakamura T., Tsuchiyama A., Akaki T., Uesugi K., Nakano T., Takeuchi A., Suzuki Y., and Noguchi T. 2008a. Bulk mineralogy

and three dimensional structures of individual Stardust particles deduced from synchrotron X-ray diffraction and microtomography analysis. *Meteoritics & Planetary Sciences* 43: 247–259.

Nakamura T., Noguchi T., Tsuchiyama A., Ushikubo T., Kita N. T., Valley J. W., Zolensky M. E., Kakazu Y., Sakamoto K., Mashio E., Uesugi K., and Nakano T. 2008b. Chondrule-like objects in short-period comet 81P/Wild 2. *Science* 321:1664–1667.

Nakano T., Nakashima Y., Nakamura K., and Ikeda S. 2000. Observation and analysis of internal structure of rock using X-ray CT. *Journal of Geological Society Japan* 106:363–378. In Japanese.

Nakano T., Tsuchiyama A., Uesugi K., Uesugi M., and Shinohara K. 2006. "Slice"—Software for basic 3-D analysis, Slice webpage http://www-bl20.spring8.or.jp/slice/, Japan Synchrotron Radiation Research Institute (JASRI).

Rietmeijer F. J. M., Nakamura T., Tsuchiyama A., Uesugi, K., and Nakano T. 2007. Origin and formation of iron-silicide phases in the aerogel of the Stardust mission. *Meteorites & Planetary Science* 43:121–134.

Sandford S. A., Aleon J., Alexander C. M. O'D. Araki T. and 51 additional authors. 2006. Organics captured from comet 81P/Wild 2 by the Stardust spacecraft. *Science* 314:1720–1724.

Trigo-Rodriguez J. M., Dominguez G., Burchell M. J., Hörz F., and Llorca J. Bulbous tracks arising from hypervelocity capture in aerogel. *Meteorites & Planetary Science* 43:75–86.

Tsou P. 1990. Intact capture of hypervelocity projectiles. *International Journal of Impact Engineering* 10:615–627.

Tsuchiyama A., Uesugi K., Nakano T., and Ikeda S. 2005. Quantitative evaluation of attenuation contrast of X-ray computed tomography images using monochromatized beams. *American Mineralogist* 90:132–142.

Uesugi K., Suzuki Y., Yagi N., Tsuchiyama A. and Nakano T. 2001. Development of high spatial resolution X-ray CT system at BL47XU in SPring-8, *Nuclear Instruments of Methods in Physics Research A* 467–468:853–856.

Uesugi K., Tsuchiyama A., Yasuda H., Nakamura M., Nakano T., Suzuki Y., and Yagi N. 2003. Micro-tomographic imaging for material sciences at BL47XU in SPring-8. *Journal de Physique IV France* 104:45–48.

Yano H., Okazaki T., Tsuchiyama A., Uesugi K., Nakano T., Noguchi T., Okudaira K., and McDonnell J. A. M. 2005. Three-dimensional structures of impact tracks and their captured dust particles in the EuReCa aerogel using SR microtomography (abstract). *Meteorites & Planetary Science* 40:A171.

Zolensky M. E., Zega T. J., Yano H., Wirick S. and 71 additional authors 2006. Mineralogy and petrology of comet 81P/Wild 2 nucleus samples. *Science* 314:1735–1739.

APPENDIX: TRACK SHAPE PARAMETERS IN COMPARISON WITH OPTICAL MICROGRAPH

The track shape parameters, such as length, width and volume, can be obtained easier by optical microscopy (OM) than by tomography. Thus, the parameters obtained by tomography are compared with those by optical micrographs to check the accuracy of the OM measurement.

The shape parameters were obtained from the optical micrographs (Fig. 1) too and are shown in Table A1. The OM track length, L'_t, is almost the same as the CT length, L_t. The OM track volume, V'_t, which was estimated by assuming cylindrical symmetry of the track, is also the same as the CT volume, V_t, except for Namekuji.

The pixel size of the projection images using the X-ray image detector was determined in SPring-8, and the precision of the voxel size of the CT image is about 1%. If the track is oblique to the triangular flat surfaces of a keystone, the apparent OM track length becomes shorter than the real length, but the 3-D CT images show that the tracks in the keystones are almost parallel to the triangular flat surfaces (i.e., perpendicular to tile surfaces, e.g., Figs. 4d–h). Aberration of optical lenses used in the optical microscopes (and also in the X-ray monitor for the tomography) may cause an error in the track length, but it is small. Another cause for discrepancy is refraction of light in the aerogels. However, according to Denilyuk et al. (2002), the refractive index of silica aerogel with $\rho = 5$ mg/cm^3 is only 1.001. Therefore, in conclusion, the track length can be measured accurately by OM, and the cylindrical shape assumption is appropriate for volume estimation by OM.

Table A1. Track shape parameters measured using an optical microscope.

Track #	Allocation	Track length, L'_t (μm)[*]	Track volume, V'_t (cm^3)[*]	L'_t/L_t	V'_t/V_t
Track 67	C2126,1,67,0 (Namekuji)	122	6.45E + 04	1.07	1.42
Track 68	C2126,2,68,0 (Skyrocket)	2686	9.36E + 06	1.01	1.02
Track 46	C2126,4,46,0 (Gobou)	929	1.81E + 05	≤0.97	≤0.92

[*]Measured by an optical microscope.
n.d.: not determined.